Supplementary Materials for

N^6-methyladenosine of chromosome-associated regulatory RNA regulates chromatin state and transcription

Jun Liu, Xiaoyang Dou, Chuanyuan Chen, Chuan Chen, Chang Liu, Meng Michelle Xu, Siqi Zhao, Bin Shen, Yawei Gao†, Dali Han†, Chuan He†

†Corresponding author. Email: chuanhe@uchicago.edu (C.H.); handl@big.ac.cn (D.H.); gaoyawei@tongji.edu.cn (Y.G.)

Published 16 January 2020 on *Science* First Release
DOI: 10.1126/science.aay6018

This PDF file includes:

Other Supplementary Material for this manuscript includes the following:
(available at science.sciencemag.org/cgi/content/full/science.aay6018/DC1)

Tables S1 and S2 (.xlsx)

Materials and Methods

Cell lines, antibodies, oligonucleotides and plasmids electroporation

Mettl3 knockout (KO) and wild type are mouse embryonic stem cells (mESCs) that were provided by Howard Y. Chang (Stanford University). *Mettl3*$^{-/-}$-1 were electroporated with PPB-CAG-m*Mettl3*-puromycin or PPB-CAG-m*Mettl3*-APPW-puromycin, 24 hours (h) after electroporation, 1 μg/ml Puromycin (Promega) was added to generate stable rescued *wt* or *mu Mettl3* mESCs. *Ythdc1* conditional knockout (CKO) and rescued *wt* or *mu Ythdc1* mESCs were generated by Bin Shen (Nanjing Medical University). Briefly, *Ythdc1* CKO cells were derived from *Ythdc1*$^{flox/flox}$ blastocyst. 2×10^5 mESC cells were transfected with 200 ng PB-CAG-Puromycin-P2A-CreERT2 and 100 ng PBase by electroporation. After 24 h, electroporated cells were treated with 1 μg/ml Puromycin to generate stable *Ythdc1*$^{flox/flox}$*; CreERT2* ES clones (*Ythdc1* CKO). *Ythdc1*$^{flox/flox}$*; CreERT2* ES cells were electroporated with PB-CAG-mYthdc1-P2A-blasticidin or PB-CAG-mYthdc1-W377A-P2A-blasticidin, 24 h after electroporation, 1 μg/ml Puromycin and 10 μg/ml blasticidin were added to generate stable rescued *wt* or *mu Ythdc1* mESCs. WT and *Zcchc8*$^{-/-}$ mESCs were gifts from Yawei Gao (Tongji University). *Ythdf2* CKO mESCs were provided by Bin Shen. To induce *Ythdc1* CKO and *Ythdf2* CKO mESCs, *Ythdc1*$^{flox/flox}$; *CreERT2* or *Ythdf2*$^{flox/flox}$; *CreERT2* mESC cells were treated with 1 μg/ml 4-hydroxytamoxifen (Sigma) for 48 h. Cells were maintained in DMEM (Invitrogen) supplemented with 15% FBS (GeminiBio), 1% nucleosides (100×) (Millipore), 1 mM L-glutamine (Gibco), 1% nonessential amino acid (Gibco), 0.1 mM 2-mercaptoethanol (Sigma), 1,000 U/ml LIF (Millipore), 3 μM CHIR99021 (Stemcell) and 1 μM PD0325901 (Stemcell) in 37 °C and 5% CO_2.

The HEC-1-A stable cell line used in this study was previously generated using the TRC Lentiviral Human shRNA system (*28*). Cells were grown in McCoy's 5A medium (Invitrogen) supplemented with 10% FBS (Gibco), and 1% Penicillin-Streptomycin (Gibco) in 37 °C and 5% CO_2.

Primary antibodies were purchased from commercial sources: rabbit anti-H3K4me3 (ab8580, Abcam); rabbit anti-H3K27ac (ab4729, Abcam); rabbit anti-Histone H3 (9715, Cell Signaling Technologies); rabbit anti-β–Tubulin (2146, Cell Signaling Technologies); rabbit anti-U1-70K (ab83306, Abcam); rabbit anti-RBM7 (ab174198, Abcam); rabbit anti-ZCCHC8 (23374-1-AP, ProteinTech); mouse HRP-anti-Flag (A8592, Sigma); rabbit anti-METTL3 (ab195352, Abcam); rabbit anti-YTHDC1 (ab122340, Abcam); rabbit anti-YTHDF2 (24744-1-AP, ProteinTech); mouse anti-RNA Polymerase II (664912, Biolegend); rabbit anti-KAT3B/p300 (ab14984, Abcam); rabbit anti-YY1 (ab109237, Abcam); rabbit anti-JARID2 (NB100-2214, Novus Biologicals); rabbit anti-ORF1p (ab216324, Abcam); rabbit anti-Orf2 (600-401-GT3S, Rockland Immunochemicals); goat HRP-anti-GAPDH (HRP-60004, ProteinTech).

The antisenses for LINE1 study used in this paper were purchased from Gene Tools (*20*). The oligonucleotide sequence for control is: 5'-CCTCTTACCTCAGTTACAATTTATA-3'; for LINE1 is: 5'-TGGCATTCTGTTCTTGTGGCTGTCT'-3'.

The PPB-CAG-m*Mettl3*-puromycin plasmid was constructed by cloning mouse *Mettl3* cDNAs into a PiggyBac Transposon System (SBI). Site-directed mutagenesis on PPB-CAG-m*Mettl3*-puromycin plasmid was done to generate PPB-CAG-m*Mettl3*-APPW-puromycin plasmid with primers: METTL3APPWFor, 5'-

AGTTGTGATGGCTGCCCCACCTTGGGATATT-3'; METTL3APPWRev, 5'-AATATCCCAAGGTGGGGCAGCCATCACAACT-3'; METTL3APPAFor: 5'-ATGGCTGCCCCACCTGCGGATATTCACATGGA-3'; METTL3APPARev: 5'-TCCATGTGAATATCCGCAGGTGGGGCAGCCAT-3'. Electroporation was achieved by using Lonza Nucleofector-4D (Lonza) following manufacturer's instructions.

DNase I-TUNEL experiment

mESCs or HEC-1-A cells were permeabilized by 0.5% Triton X-100 in PBS buffer (Invitrogen) for 15 min before digesting with 0.2 U/ml of DNase I (NEB). Cells were then fixed in 4% PFA. TUNEL Assays (DeadEnd™ Fluorometric TUNEL System, Promega) were performed subsequently according to manufacturer's instructions. The nuclear area was defined according to DAPI DNA staining. Images were captured with Olympus FV1000 confocal and intensity of nuclear TUNEL signal was quantified using Image J software. Flow cytometry was performed on a BD Fortessa (BD) and data was analyzed using Flowjo (Treestar).

Nascent RNA labeling assay

mESCs or HEC-1-A cells were cultured on pre-coated glass over slides. 24 h later, a nascent RNA synthesis assay was conducted using Click-It RNA Imaging Kits (Invitrogen, C10329) following the manufacturer's protocols. Images were captured with Olympus FV1000 confocal and intensity of signal was quantified using Image J software.

Western blot

Samples were homogenized in RIPA buffer (Invitrogen) containing 1 × protease inhibitor cocktail and 1 × phosphatase inhibitor cocktail (Sigma). Lysates were boiled at 95 °C with 4 × loading buffer (Biorad) for 5 min and then stored at –80 °C for use in the next step. A total of 30 μg protein per sample was loaded into 4-12% NuPAGE Bis-Tris gel and transferred to PVDF membranes (Life Technologies). Membranes were blocked in 5% milk PBST for 30 min at room temperature (RT), incubated in a diluted primary antibody solution at 4 °C overnight, washed and incubated in a dilution of secondary antibody conjugated to HRP for 1 h at RT. Protein bands were detected using SuperSignal West Dura Extended Duration Substrate kit (Thermo) and FluroChem R (Proteinsimple).

Cell fractionation

mESCs or HEC-1-A cells were fractionated according to a previously published procedure (*29*). Briefly, 5×10^6 to 1×10^7 cells were collected and washed with 1 mL cold PBS/1 mM EDTA buffer, then centrifuged at RT with 500 g to collect the cell pellet. 200 μL ice cold lysis buffer (10 mM Tris-HCl, pH = 7.5, 0.05% NP40, 150 mM NaCl) were added to the cell pellet and incubated on ice for 5 min, then gently pipetted up the cell lysate over 2.5 volumes of chilled sucrose cushion (24% RNase-free sucrose in lysis buffer) and centrifuged at 4 °C with 15,000 g for 10 min. Collected all the supernatant as cytoplasmic fraction. Gently added 200 μL ice cold PBS/1mM EDTA to the nuclei pellet without dislodging the pellet, then aspirated the PBS/EDTA. The nuclei pellet were resuspended in 200 μL prechilled glycerol buffer (20 mM Tris-HCl, pH = 7.9, 75 mM NaCl, 0.5 mM EDTA, 0.85 mM DTT, 0.125 mM PMSF, 50% glycerol) with gentle flicking of the tube, then added equal volume of cold nuclei lysis buffer (10 mM HEPES,

pH = 7.6, 1 mM DTT, 7.5 mM $MgCl_2$, 0.2 mM EDTA, 0.3 M NaCl, 1 M UREA, 1% NP-40) then vortexed vigorously for 2 × 5 seconds. The nuclei pellet mixtures were incubated for 2 min on ice, then centrifuged at 4 °C with 15,000 g for 2 min. The supernatant was collected as soluble nuclear fraction/nucleoplasm, pellet was gently rinsed with cold PBS/1 mM EDTA without dislodging then collected as chromosome-associated fraction.

RNA isolation

Total RNA was isolated with TRIZOL reagent (Invitrogen). Nonribosomal RNA was extracted from the total RNA using the RiboMinus transcriptome isolation kit (Invitrogen) following the manufacturer's protocols. RNA concentration was measured by UV absorbance at 260 nm. Total RNA samples used for RT-qPCR were isolated by using the RNeasy kit (Qiagen) with an additional on-column DNase-I digestion step.

LC-MS/MS quantification of m^6A in nonribosomal RNA

100 ng of nonribosomal RNA was digested by nuclease P1 (1 U) in 25 μL of buffer containing 20 mM of NH4Ac at 42 ºC for 2 h, followed by the addition of NH_4HCO_3 (1 M, 3 μL) and alkaline phosphatase (0.5 U), then incubation at 37 ºC for 2 h. The sample was then filtered (0.22 μm pore size, 4 mm diameter, Millipore), and 5 μL of the solution was injected into the LC-MS/MS. The nucleosides were separated by reverse phase ultra-performance liquid chromatography on a C18 column with online mass spectrometry detection using Agilent 6410 QQQ triple-quadrupole LC mass spectrometer in positive electrospray ionization mode. The nucleosides were quantified by using the nucleoside to base ion mass transitions of 282 to 150 (m^6A), and 268 to 136 (A). Quantification was performed by comparison with a standard curve obtained from pure nucleoside standards run with the same batch of samples. The ratio of m^6A to A was calculated based on the calibrated concentrations.

Chromosome-associated RNA m^6A-seq

Total RNA was isolated from the chromosome-associated fraction of mESCs or human HEC-1-A cells. Nonribosomal RNA was further enriched from total RNA by using RiboMinus transcriptome isolation kit (Invitrogen). 1 μL 1:1000 diluted m^6A spike-in from EpiMark N6-Methyladenosine Enrichment Kit (NEB #E1610S) was added to 1 μg nonribosomal caRNA, followed by fragmentation according to previously published protocols (*1*). m^6A-IP was performed using EpiMark N^6-Methyladenosine Enrichment Kit following the manufacturer's protocols. Library preparation was performed by using SMARTer Stranded Total RNA-Seq Kit v2 (Takara) according to the manufacturer's protocols. Sequencing was performed at Berry Genomics (China) on an Illumina NovaSeq machine in pair-end mode with 150 base pair (bp) per read.

Chromosome-associated RNA m^6A-seq analysis

Raw reads were trimmed with Trimmomatic-0.38 (*30*), then aligned to the mouse genome and transcriptome (mm10, version M19, 2018-08-30), or human genome and transcriptome (hg38, version 29, 2018-08-30), together with spike-in genomes including unmodified control RNA (Cypridina Luciferase) and m^6A methylated control RNA (Gaussia Luciferase) (New England Biolabs) using HISAT (version 2.1.0) (*31*) with '--rna-

strandness RF' parameters. Annotation files (version M19, 2018-08-30, in gtf format for mouse; or version 29, 2018-08-30, in gtf format for human) were downloaded from GENCODE database (https://www.gencodegenes.org/). Mapped reads were separated by strands with samtools (version 1.9) (*32*) and m^6A peaks on each strand were called using MACS (version 2) (*33*) with parameter '--nomodel' and '--keep-dup 5' separately. Significant peaks with $q < 0.01$ identified by MACS2 were considered. Peaks identified in at least two biological replicates were merged using bedtools (v.2.26.0) (*34*) and were used in the following analysis. The number of reads mapped to mouse or human genome divided by number of reads mapped to m^6A modified spike-in represented whole m^6A level. Two methods were used to quantify the reproducibility of two biological replicates. 1) Venn diagram showing number of m^6A peaks shared by two biological replicates. 2) Pearson correlation coefficiency of m^6A level on union peaks called by two biological replicates.

YTHDC1 co-immunoprecipitation

mESCs stably expressed FLAG-tagged YTHDC1 or vector Control were collected by scraping, pelleted, and washed twice using PBS. Cells were resuspended with lysis buffer (25 mM Tris-HCl, pH = 7.2, 150 mM NaCl, 5 mM $MgCl_2$, 1% NP40, 5% glycerol), incubated on ice for 10 min and sonicated for 1 min. The lysate was centrifuged at 4℃ for 30 min with 13,000 rpm, and the supernatant was recovered. 50 μL of supernatant were saved as input. The remaining supernatant was incubated with anti-Flag M2 magnetic beads (Sigma) for 4 h at 4℃, then with elution buffer (0.5 mg/ml 3xFlag peptide in lysis buffer) for 1.5 h at 4℃. Eluted and input samples were treated with SDS loading buffer for 5 min at 95 ℃, then analyzed by western blotting.

RNA-seq for nuclear nonribosomal RNA decay

Six 6-cm plates of mESCs were seeded and controlled to afford the same amount of cells. After 48 h, actinomycin D was added to 5 $\mu g\,ml^{-1}$ at 6 h, 3 h, and 0 h before trypsinization collection. The nuclear fraction was separated and total RNA was purified by Trizol. Before purified nonribosomal RNA with RiboMinus transcriptome isolation kit, ERCC RNA spike-in control (Ambion) was added to each sample (0.1 μl per sample). Library preparation was performed by using SMARTer Stranded Total RNA-Seq Kit (Takara) v2 according to the manufacturer's protocols. Sequencing was performed at the University of Chicago Genomics Facility on an Illumina NextSeq 500 machine in pair-end mode with 50 bp per read.

Half lifetime nuclear RNA-seq analysis

Raw reads were trimmed with Trimmomatic-0.38 (*30*), then aligned to mouse genome and transcriptome (mm10, version M19, 2018-08-30) and external RNA Control Consortium (ERCC) RNA spike-in control (Thermo Fisher Scientific) using HISAT (version 2.1.0) (*31*) with '--rna-strandness RF' parameters. Annotation files (version M19, 2018-08-30, in gtf format) were downloaded from GENCODE database (https://www.gencodegenes.org/). Reads on each GENCODE annotated gene were counted using HTSeq (*35*) and then normalized to counts per million (CPM) using edgeR (*36*) packages in R. CPM was converted to attomole by linear fitting of the RNA ERCC spike-in. Half lifetime of RNA was estimated using formula listed in previously published

paper (*37*). Specifically, as actinomycin D treatment results in transcription stalling, the change of RNA concentration at a given time (dC/dt) is proportional to the constant of RNA decay (K_{decay}) and the RNA concentration (C), leading to the following equation:

$$\frac{dC}{dt} = -K_{decay}C$$

Thus, the RNA degradation rate K_{decay} was estimated by:

$$\ln\left(\frac{C}{C_0}\right) = -K_{decay}t$$

To calculate the RNA half-life ($t_{1/2}$), when 50% of the RNA is decayed (that is, $\frac{C}{C_0} = \frac{1}{2}$), the equation was:

$$\ln\left(\frac{1}{2}\right) = -K_{decay}t_{\frac{1}{2}}$$

From where:

$$t_{\frac{1}{2}} = \frac{ln2}{K_{decay}}$$

The final half-life was calculated by using the average value of 0 h, 3 h and 6 h.

Nuclear RNA-seq data analysis

Raw reads were trimmed with Trimmomatic-0.38 (*30*), then aligned to mouse genome and transcriptome (mm10, version M19, 2018-08-30), or human genome and transcriptome (hg38, version 29, 2018-08-30), together with external RNA Control Consortium (ERCC) RNA spike-in control (Thermo Fisher Scientific) using HISAT (version 2.1.0) (31) with '--rna-strandness RF' parameters. Annotation files (version M19, 2018-08-30, in gtf format for mouse; or version 29, 2018-08-30, in gtf format for human) were downloaded from GENCODE database (https://www.gencodegenes.org/). Reads on each GENCODE annotated gene were counted using HTSeq (*35*) and then normalized to counts per million (CPM) using edgeR (*36*) packages in R. CPM was converted to attomole by linear fitting of the RNA ERCC spike-in. Differentially expressed genes (DEGs) with P value < 0.05 and fold changes (FC) > 2 were identified using two-sided Student's t test.

Quantification of RNA methylation with m^{6}A-IP and RT-qPCR

We performed m^{6}A-IP enrichment followed by RT-qPCR to quantify the changes to m^{6}A methylation level change of a certain target m^{6}A site. 0.5 μg purified nonribosomal caRNA extracted from mESCs was added 1 μL 1:100 diluted m^{6}A and non-m^{6}A spike-in from EpiMark N6-Methyladenosine Enrichment Kit (NEB #E1610S), then performed m^{6}A-IP using EpiMark N6-Methyladenosine Enrichment Kit following the manufacturer's protocols. RNA was extracted from IP and Input fractions by acid phenol/chloroform extraction, then subjected to RT-qPCR. The spike-in was used as a reference gene when performing qPCR.

RNA lifetime measurement by qPCR

Six 6-cm plates of mESCs were seeded and controlled to afford the same amount of cells. After 48 h, actinomycin D was added to 5 μg ml^{-1} at 6 h, 3 h, and 0 h before trypsinization collection. The nuclear fraction was separated and total RNA was purified by Trizol. Before RNA quantities were determined by RT-qPCR, 1 μL 1:100 diluted m^{6}A and non-m^{6}A spike-in from EpiMark N6-Methyladenosine Enrichment Kit (NEB #E1610S) was added.

The degradation rate of RNA (k) was estimated by plotting N_t/N_0 against time and fitting to the following equation:

$$\frac{N_t}{N_0} = e^{-kt}$$

where t is the transcription inhibition time, and N_t and N_0 are the RNA quantities at time t and time 0. The RNA lifetime ($t_{1/2}$) can be calculated from the degradation rate as follows:

$$t_{\frac{1}{2}} = \frac{ln2}{k}$$

RT-qPCR

Quantitative reverse transcription PCR (RT-qPCR) was used to assess the relative abundance of RNA. Total RNA or purified nonribosomal RNA was reverse transcribed with PrimeScript RT Reagent Kit (Takara) using poly(dA) and random primers to obtain cDNA. qPCR was performed by using FastStart Essential DNA Green Master (Roche). m^{6}A and non-m^{6}A spike-in from EpiMark N6-Methyladenosine Enrichment Kit were used as control. Primers used for RT-qPCR are listed in **Table S1.** Relative changes in expression were calculated using the $\Delta\Delta C_t$ method.

RNA-seq for transcription rate

Eight 6-cm plates of mESCs or human HEC-1-A cells were seeded and controlled to afford the same amount of cells. After 48 h, 5-Ethynyl Uridine (EU) was added to 0.5 mM at 60 min, 30 min, 20 min and 10 min before trypsinization collection. Total RNA was purified by Trizol and nascent RNA was captured by using Click-iT Nascent RNA Capture Kit (Invitrogen). Before constructing libraries with SMARTer Stranded Total RNA-seq Kit (Takara) v2, ERCC RNA spike-in control (Ambion) was added to each sample (0.01 μl per sample). Sequencing was performed at the University of Chicago Genomics Facility on an Illumina HiSeq 4000 machine in single-read mode with 50 bp per read.

Nascent RNA-seq data analysis

Raw reads were trimmed with Trimmomatic-0.38 (*30*), then aligned to mouse genome and transcriptome (mm10, version M19, 2018-08-30) or human genome and transcriptome (hg38, version 29, 2018-08-30), together with external RNA Control Consortium (ERCC) RNA spike-in control (Thermo Fisher Scientific) using HISAT (version 2.1.0) (*31*) with '--rna-strandness R' parameters. Annotation files (version M19, 2018-08-30, in gtf format for mouse; or version 29, 2018-08-30, in gtf format for human) were downloaded from GENCODE database (https://www.gencodegenes.org/). Reads on each GENCODE

annotated gene were counted using HTSeq (*35*) and then normalized to counts per million (CPM) using edgeR (*36*) packages in R. CPM was converted to attomole by linear fitting of the RNA ERCC spike-in. RNA level and EU adding time was fitted to linear equation, and the slope was estimated as transcription rate of RNA.

Nascent RNA transcription rate measurement by qPCR

Eight 6-cm plates of mESCs were seeded and controlled to afford the same amount of cells. After 48 h, 5-Ethynyl Uridine (EU) was added to 0.5 mM at 60 min, 30 min, 20 min and 10 min before trypsinization collection. Total RNA was purified by Trizol and nascent RNA was captured by using Click-iT Nascent RNA Capture Kit (Invitrogen). Before RNA quantities were determined by RT-qPCR, 1 μL 1:100 diluted m^6A and non-m^6A spike-in from EpiMark N6-Methyladenosine Enrichment Kit (NEB #E1610S) was added. RNA amount and EU adding time was fitted to linear equation, and the slope was estimated as transcription rate of RNA.

Histone modification ChIP-seq

mESCs or human HEC-1-A cells were resuspended in growth media with a concentration of 10^6 ml^{-1}, cross-linked by adding 1% formaldehyde directly to the media and slowly shook 10 min at RT. Cross-linking was stopped by adding glycine to a final concentration of 0.125 M and incubating for 5 min at RT with a slow shake. The media was removed and the cells were washed twice with ice-cold PBS. Chromatin immunoprecipitation was performed using Auto iDeal ChIP-seq kit for Histone (diagenode) with spike-in Chromatin (Active Motif) and spike-in Antibody (Active Motif) following the manufacturer's protocols. Library preparation was performed by using KAPA HyperPlus Kits (Kapa biosystems) according to the manufacturer's protocols. Sequencing was performed at the University of Chicago Genomics Facility on an Illumina HiSeq 4000 machine in single-read mode with 83 bp per read.

METTL3 and TF ChIP-seq

mESCs were resuspended in growth media with a concentration of 10^6 ml^{-1}, cross-linked by adding 1% formaldehyde directly to the media and slowly shook 20 min at RT. Cross-linking was stopped by adding glycine to a final concentration of 0.125 M and incubating for 5 min at RT with a slow shake. The media was removed and the cells were washed twice with ice-cold PBS. The cells were then collected in lysis buffer (0.1% SDS, 2 mM EDTA, 1 x protease inhibitors, 20 mM Tris–HCl, pH = 8.0, 150 mM NaCl, 1% Triton) and the lysates were sonicated by a Bioruptor UCD-200 (Diagenode) to result in DNA fragments of 200 to 500 bp in length (for TF ChIP-seq, spike-in chromatin (Active Motif) was added in before sonication). Cellular debris was removed by centrifugation and the lysates were diluted 1:10 in ChIP dilution buffer (0.01% SDS, 1.1% Triton X-100, 1.2 mM EDTA, 167 mM NaCl, 1 x protease inhibitors, 16.7 mM Tris–HCl, pH = 8.0). 1% of sonicated chromatin was used as Input control. Washed Protein G Magnetic beads (Invitrogen) two times with ChIP buffer, eluted beads in 1 mL of ChIP buffer, added antibody (for TF ChIP-seq, spike-in antibody (Active Motif) was used) and incubated the mixture 2 h on rotating platform at 4 °C. Then washed the antibody-coated beads with ChIP buffer three times. Chromatin solutions were incubated overnight at 4 °C with rotation with antibodies-coated beads. The beads were washed sequentially for 3 min by rotation with

1 ml of the following buffers: low salt wash buffer (0.1% SDS, 1% Triton X-100, 2 mM EDTA, 150 mM NaCl, 20 mM Tris–HCl, pH = 8.0), high salt wash buffer (0.1% SDS, 1% Triton X-100, 2 mM EDTA, 500 mM NaCl, 20 mM Tris–HCl, pH = 8.0) and LiCl wash buffer (0.25 M LiCl, 1% NP-40, 1% sodium deoxycholate, 1 mM EDTA, 10 mM Tris–HCl, pH = 8.0). Finally, the beads were washed twice with 1 ml TE buffer (1 mM EDTA, 10 mM Tris–HCl, pH = 8.0). The immuno-complexes and Input were then eluted by adding 400 µl of elution buffer (100 mM NaHCO3, 1% SDS) plus 18 µl 5 M NaCl and incubated for 4 h at 65 °C to reverse protein-DNA crosslinks. The remaining proteins were digested by adding 5 µl of proteinase K (Promega) and incubated overnight at 65 °C. The DNA was recovered by phenol/chloroform/isoamyl alcohol (25: 24: 1) extractions and precipitated with 0.1 volume of 3 M sodium acetate, pH = 5.2, and 3 volumes of ethanol using glycogen as carrier. Library preparation was performed by using KAPA HyperPlus Kits (Kapa biosystems) according to the manufacturer's protocols. Sequencing was performed at the University of Chicago Genomics Facility on an Illumina HiSeq 4000 machine in single-read mode with 83 bp per read.

ChIP-seq data analysis

Raw reads were trimmed with Trimmomatic-0.38 (*30*), then uniquely mapped to mouse genome (mm10, version M19, 2018-08-30) or human genome (hg38, version 29, 2018-08-30), together with Drosophila melanogaster chromatin (Spike-in Chromatin) using bowtie (version 1.2.2) (*38*) allowing one mismatch. Annotation files (version M19, 2018-08-30, in gtf format for mouse; or version 29, 2018-08-30, in gtf format for human) were downloaded from GENCODE database (https://www.gencodegenes.org/). Both H3K27ac, H3K4me3 and TF binding level were normalized by sequencing depth and spike-in Drosophila melanogaster chromatin. Histone modification peaks were called using HOMER (*39*) with '-size 1000 -minDist 1000 -F 2 -L 0' parameters. Super-Enhancer were called by ROSE (*40*) with default parameters using H3K27ac ChIP-seq data. METTL3 peaks were called using HOMER (*39*) in factor style with '-F 1 -L 1 -LP 0.001' parameters. TF peaks for EP300/YY1/JARID2 were called using HOMER (*39*) in factor style with '-F 2 -L 2' parameters. Peaks identified in at least two biological replicates were pooled using bedtools (v.2.26.0) (*34*) and were used in further analysis.

Quantification of histone mark levels with ChIP-qPCR

We performed ChIP for H3K4me3 and H3K27ac followed by qPCR to quantify the changes to histone mark level at certain regions. mESCs were resuspended in growth media with a concentration of 10^6 ml^{-1}, cross-linked by adding 1% formaldehyde directly to the media and slowly shook 10 min at RT. Cross-linking was stopped by adding glycine to a final concentration of 0.125 M and incubating for 5 min at RT with a slow shake. The media was removed and the cells were washed twice with ice-cold PBS. Chromatin immunoprecipitation was performed using Auto iDeal ChIP-seq kit for Histone (diagenode) with spike-in Chromatin (Active Motif) and spike-in Antibody (Active Motif) following the manufacturer's protocols. DNA extracted from IP and Input fractions were used to do qPCR. The spike-in was used as reference genes when performing qPCR.

mNET-seq method and RNA library preparation

mNET-seq was performed according to a published procedure (*21, 22*). Briefly, approximately $1.6x10^8$ mESCs were washed with ice-cold PBS twice. The cells were lysed with ice-cold 4 ml HLB/NP40 buffer (10 mM Tris-Hcl, pH 7.5, 10 mM NaCl, 0.5% NP40, and 2.5 mM MgCl2) and incubated on ice for 5 min. After the incubation, 1 ml of ice-cold HLB/NP40/Sucrose buffer (10 mM Tris-HCl pH 7.5, 10 mM NaCl, 0.5% NP40, 2.5 mM MgCl2, and 10% Sucrose) was under-laid and then the nuclei were collected under 1,400 rpm centrifuge at 4 ºC for 5 min. Isolated nuclei were resuspended in 125 µl of NUN1 solution (20 mM Tri-HCl, pH 8.0, 75 mM NaCl, 0.5 mM EDTA, 50% Glycerol and proteinase inhibitor 1xComplete (Roche)) followed by 1.2 ml NUN2 buffer (20 mM HEPES-KOH pH 7.6, 7.5 mM MgCl2, 0.2 mM EDTA, 300 mM NaCl, 1 M Urea, 1% NP40, proteinase inhibitor 1xComplete and phosphatase inhibitor 1xPhosStop (Roche)). 15 min incubation was carried out on ice with mixing by max speed vortex for 5 s every 4 min and then chromatin pellets were precipitated under 13,000 rpm centrifuge at 4 ºC for 10 min. Isolated chromatins were washed in 100 µl of 1x Micrococcal Nuclease (MNase) buffer (NEB) and then incubated with MNase (40 u/ml) on Thermomixer (eppendorf, 1,400 rpm) at 37 ºC for 90 s. In order to inactivate MNase, EGTA (25 mM) was added immediately after the reaction and soluble-digested chromatins were collected by 13,000 rpm centrifuge for 5 min. The supernatant was diluted with 9 ml of NET-2 buffer (50 mM Tris-HCl, pH 7.4, 150 mM NaCl, 0.05% NP40) and Pol II antibody-conjugated beads were added. 40 µg of Pol II antibody was used for each mNET-seq experiment. Immunoprecipitation was performed at 4 ºC for 1 hr. The beads were washed with 1ml of NET-2 buffer six times and with 500 µl of 1xPNKT (1xPNK buffer and 0.1% Triton X-100) buffer once in the cold room. The washed beads were incubated in 100 µl of PNK reaction mix (1xPNKT, 1 mM ATP and 0.05 U/ml T4 PNK 3' phosphatase minus (NEB) on Thermomixer (1,400 rpm) at 37 ºC for 6 min. After, the reaction beads were washed with 1ml of NET-2 buffer once and RNA was extracted with Trizol reagent. RNA was resolved on 8% denaturing acrylamide 7M urea gels for size purification. 35–100 nt fragments were eluted from the gel using RNA elution buffer (1 M NaOAc and 1 mM EDTA) and RNA was precipitated in 75% ethanol. RNA libraries were prepared according to the manual of NEBNext Multiplex Small RNA Library Prep Set for Illumina (New England Biolabs). Sequencing was performed at the University of Chicago Genomics Facility on an Illumina HiSeq 4000 machine in single-read mode with 50 bp per read.

mNET-seq data analysis

Raw reads were trimmed with Trimmomatic-0.38 (*30*), then aligned to mouse genome and transcriptome (mm10, version M19, 2018-08-30) using HISAT (version 2.1.0) (*31*) with '--rna-strandness F' parameters. Annotation files (version M19, 2018-08-30, in gtf format) were downloaded from GENCODE database (https://www.gencodegenes.org/). Elongation phase of transcription was quantified with Escaping Index (EI) which is defined as the proportion of Pol II on gene body (the interval [TSS+500, TES]) divided by that around TSS (the interval [TSS-50, TSS+250]) (*22*). El matrix was further normalized upon quantiles.

Regulatory region definition

Promoter was identified as regions upstream 1 kb of TSS and downstream 100 bp; enhancer was identified as H3K27ac peak distal from promoter (+/- 50kb to +/- 5kb of TSS) and

H3K27ac peaks were called with H3K27ac ChIP-seq in mESCs or human HEC-1-A cells using HOMER (*39*). Repeat annotation (RepeatMasker, 2019-01-29) was downloaded from UCSC Table Browser. Enhancer RNA (eRNA), promoter-associated RNA (paRNA) and repeat RNA were defined as RNA derived from enhancer, promoter and repeats, respectively. To exclude potential noises from the nascent pre-mRNA in our analysis, we further categorized paRNAs into sense (paRNA [+]; coding strand) and antisense paRNAs (paRNA [-]; template strand) based on the origins of transcripts. featureCounts (*41*) function in R were used to count reads on carRNAs including eRNA, paRNA and repeat RNA. m^6A level, transcript abundance and half lifetime of those carRNAs were normalized and calculated as described above. Mean divergence of each repeat copy within each subfamily annotated in RepeatMasker file were used to represent the evolution age of L1 subfamily. Consensus sequences of 5'UTR, ORF2 and 3'UTR of L1MdF_I, one subfamily of L1, were downloaded from Dfam (*42*) (https://dfam.org/home) and were used as reference genome to map m^6A-seq reads. Each of 5' UTR, ORF2 and 3'UTR were binned into 100 pieces and m^6A levels on each bin were quantified as $\log_2$(IP/Input) after normalized by sequence depth and spike-in.

Enrichment analysis

Motif enrichment analysis was performed with HOMER (*39*) in RNA mode, and GO enrichment analysis was performed with DAVID (*43, 44*) with default parameter.

dCas13b-FTO reporter assay

dCas13b plasmid was a gift from Dr. Bryan Dickson (University of Chicago). dCas13b-*wt* FTO plasmid was generated according to previously published procedures (*27*) with primers: ass-fto-F, 5'-TGGATCCGGCGGCTCCATGAAGCGCGTCCAGACC-3'; ass-dcas13b-R, 5'-GGTCTGGACGCGCTTCATGGAGCCGCCGGATCCA-3'; ass-dcas13b-F, 5'-AGCTGCTGGAAGCAAGATCCGGATCCGATTACAAGGACGACG-3'; ass-fto-R, 5'-CGTCGTCCTTGTAATCGGATCCGGATCTTGCTTCCAGCAGCT-3'. Site-directed mutagenesis on the dCas13b-*wt* FTO plasmid was performed to generate dCas13b-*mu* FTO (inactive) plasmid using primers: dCas13b-mFTO-For, 5'-GTGAGCTGGGCTCACGCTGAGAACCTGGTGGAC-3'; dCas13b-mFTO-Rev: 5'-GTCCACCAGGTTCTCAGCGTGAGCCCAGCTCAC-3'. The plasmids were sequenced by the University of Chicago Comprehensive Cancer Center DNA Sequencing and Genotyping Facility. gRNA sequences are listed in **Table S1**.

Cell proliferation assay

5000 cells were seeded per well in a 96-well plate. The cell proliferation was assessed by assaying cells at various time points using the CellTiter 96® Aqueous One Solution Cell Proliferation Assay (Promega) following the manufacturer's protocols. For each sample tested, the signal from the MTS assay was normalized to the value observed at ~5 or 24 h after seeding.

Wound healing assay

Cells were seeded on collagen I-coated six-well culture dishes at a density of $1x10^6$ cells/well in media without serum to prevent cell proliferation and induce migration. A wound was made in the center of the culture 24 h after seeding, and cells were imaged

directly after making the wound and 48 h later. Migration distance was calculated as follows:

$$\frac{w_0 - w_{48}}{2w_0}$$

where w_0 is the width of the wound at time zero and w_{48} is the width of the wound after 48 h.

EB assay

mESCs were trypsinized and a total of $1x10^5$ cells per well were cultured in ultra-low cluster plates (Costar) in DMEM (Gibco) supplemented with 15% FBS (Gibco), 1mM L-glutamine (Gibco), 0.1mM mercaptoethanol (Sigma), 1% nonessential amino acid (Gibco). EBs were collected and counted every 24 h after seeded until four days. Total RNA of EBs was extracted and analyzed for the marker genes using RT-qPCR.

Statistics and reproducibility

At least three biological replicates were used in each experiment unless otherwise stated. Data are presented as the mean ± standard error of the mean (s.e.m.) or standard deviation (s.d.). Two-tailed Student's *t*-tests or non-parametric Wilcoxon-Mann–Whitney test (Wilcoxon rank-sum test, two-sided) were applied for calculating the *P* value indicated in the figure legends were performed to assess the statistical significance of differences between groups. Pearson correlation coefficients (PCC) were calculated to assess correlation. For box plots, the center line represents the median, the box limits show the upper and lower quartiles, whiskers represent 1.5x the interquartile range. In order to evaluate the scatter of the data points around the fitted regression line, R^2 is used in our scatter plots which indicates the percentage of the dependent variable variation that a linear model explains

Public datasets

One data set from NCBI's s Gene Expression Omnibus (GEO) with GSE numbers GSE61997 were downloaded and analyzed in this study (fig. S19A) (*11*).

Data availability

The m^6A-seq, half lifetime nuclear RNA-seq, nuclear RNA-seq, nascent RNA-seq, mNET-seq and ChIP-seq data generated by this study have been deposited in the GEO database under the accession number GSE133600 (mESC) and GSE140561 (HEC-1-A). Sample information are provided in **Table S2.**

Supplementary Text

Decay of LINE1 regulated by YTHDC1 and METTL3

A representative young subfamily of LINE1, L1Md_F, was analyzed. The ORF2 of L1Md_F exhibits a relatively even distribution of m^6A peaks, except for a slight enrichment around 5'UTR (fig. S6G). We examined m^6A levels on L1Md_F RNA by m^6A immunoprecipitation (m^6A-IP) followed by RT-qPCR, verifying that the methylation level of L1Md_F decreased in *Mettl3* KO mESCs, and increased in *Ythdc1* CKO mESCs versus controls (fig. S7, A and B). LINE1 RNA also displayed an increased abundance and longer

half lifetime upon *Ythdc1* or *Mettl3* depletion (fig. S7, C to G). These changes in m^6A level and half lifetime were restored in *Ythdc1* or *Mettl3* depleted cells by expressing the corresponding WT cDNAs, but not the mutant versions proteins (fig. S7), respectively. Thus, YTHDC1 regulates the decay of a portion of carRNAs, in particular LINE1 RNA, in an m^6A-dependent manner.

carRNA regulation roles in endometrial cancer progression

We have previously found that AKT activation promotes the aggressive proliferation phenotypes of the METTL3-low endometrial cancer cells but there are other unidentified METTL3-dependent pathways also involved (*28*). Consistent with our observation in mESCs, *METTL3* knockdown in HEC-1-A cells decreased the m^6A level of carRNAs and induced transcription activation and chromatin openness (fig. S20, A to E). Transcript abundances of m^6A-modified carRNAs also increased upon *METTL3* knockdown (fig. S20, F and G). When we ranked repeats families according to their m^6A fold changes upon *METTL3* knockdown, LINE1 and Alu were identified among the most responsive ones (fig. S20H). We performed time-course RNA-seq of nascent transcripts as well as total nuclear RNA-seq in control and *METTL3* knockdown HEC-1-A cells, and consistently, we observed global increases in both nuclear gene expression and transcription rate in *METTL3* knockdown cells. Moreover, genes with m^6A-marked upstream carRNAs showed higher increase in transcription rate than those with non-m^6A-marked upstream carRNAs (fig. S21, A to C). We observed upregulation of transcription for genes whose upstream carRNAs showed reduced methylation upon *METTL3* knockdown (fig. S21D); those genes with reduced upstream carRNAs methylation ($\log_2FC < -1.58$) and increased transcription rate ($\delta > 1.3$) are mainly involved in chromatin modification, cell migration and cell proliferation (fig. S21E). The seRNAs are also regulated by m^6A and affect downstream gene transcription (fig. S22). We further confirmed the activation of two active histone marks in *METTL3* knockdown cells in an m^6A-dependent manner according to ChIP-seq of H3K4me3 and H3K27ac (fig. S23, A and B). We speculate that the increased chromatin accessibility induced by reduced m^6A on carRNAs could contribute to migration of *METTL3* knockdown endometrial cancer cells. We treated both control and *METTL3* knockdown HEC-1-A cells with HDAC inhibitor (HDACi), respectively, and as expected, the increased cell migration in *METTL3* knockdown cells was restored by HDACi treatment down to a similar level to that in control cells (fig. S23C).

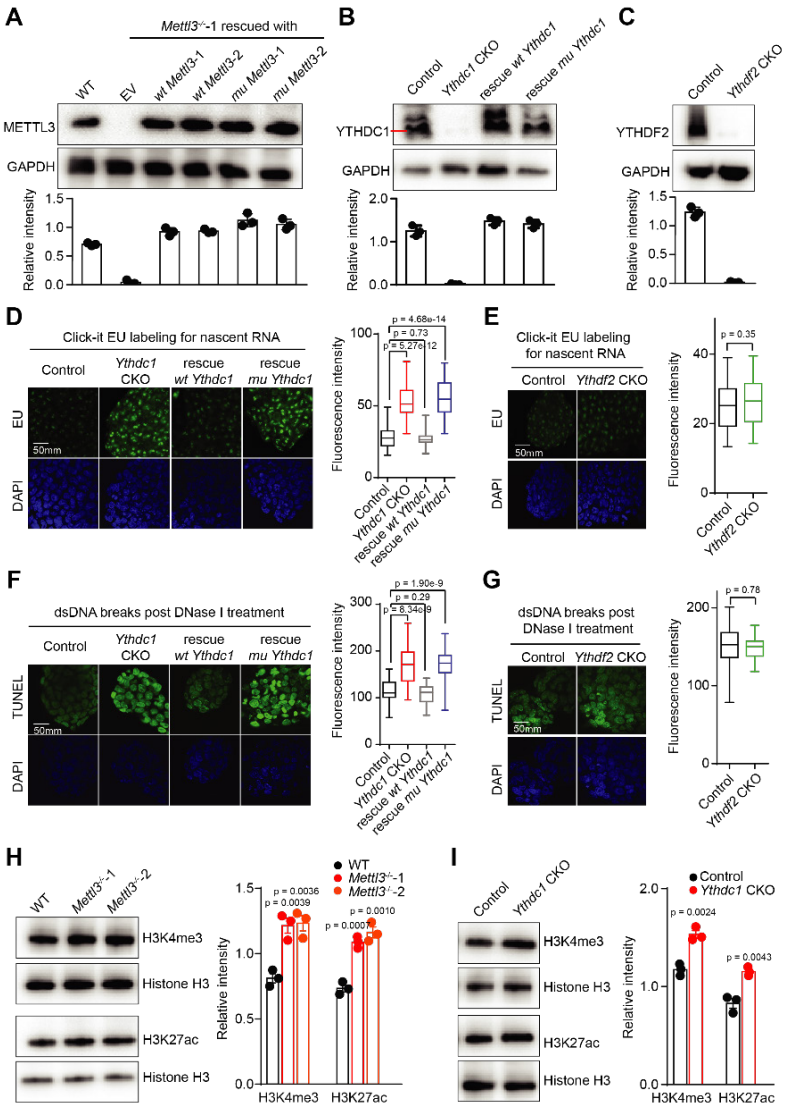

Fig. S1. The m^{6}A reader YTHDC1 regulates nascent RNA transcription and chromatin accessibility in mESCs. (**A** to **C**) Immunoblot assays showing METTL3 protein level in *Mettl3* KO and rescue with WT and inactive mutant METTL3 (A), YTHDC1 level in *Ythdc1* CKO and rescue with WT and inactive mutant YTHDC1 (B), and YTHDF2 level in *Ythdf2* CKO (C) mESCs compared with the controls. The protein levels were quantified by normalized to GAPDH protein level. EV, empty vector, referring to *Mettl3*$^{-/-}$ mESCs when transfected with empty vector plasmid. (**D** and **E**) Nascent RNA syntheses in *Ythdc1* (D) or *Ythdf2* (E) CKO mESCs versus their controls were detected by a click-it RNA Alexa fluor 488 imaging kit. *Ythdc1* CKO mESCs were rescued with the WT or a mutant YTHDC1 defected in m^{6}A recognition (D). (**F** and **G**) Analysis of chromatin accessibility in *Ythdc1* (F) and *Ythdf2* (G) CKO mESCs versus their controls by DNase I-TUNEL assay. *Ythdc1* CKO mESCs were rescued with the wild-type or the mutant YTHDC1 (F). For (D) to (G), nucleus is counterstained by DAPI. (**H-I**) Immunoblot assays showing increased global histone H3K4me3 and H3K27ac levels in *Mettl3* (H) and *Ythdc1* (I) depleted mESCs compared with the controls. The changes of H3K4me3 and H3K27ac level were quantified by normalized to the H3 level.

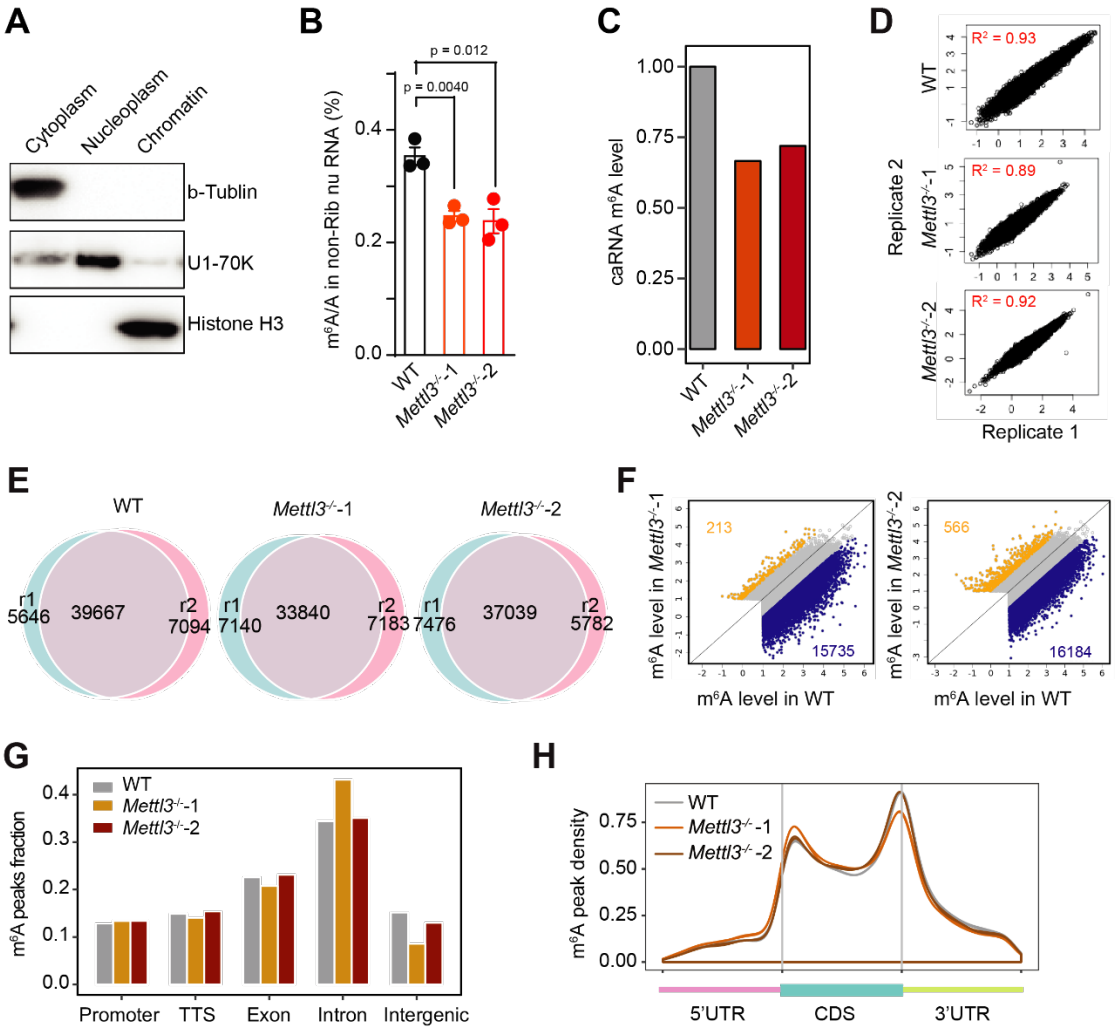

Fig. S2. The RNA m^{6}A methylation levels are different in *Mettl3*$^{-/-}$ and WT mESCs. (**A**) Cell fractionation validation shown by Western blots analysis. (**B**) LC-MS/MS quantification of the m^{6}A/A ratio in nonribosomal RNA extracted from soluble nucleoplasmic cell fraction of WT or *Mettl3*$^{-/-}$ mESCs. n = 3 biological replicates. Error bars indicate mean ± S.E.M. P values were determined by two-tailed t test. (**C**) m^{6}A levels of caRNAs in *Mettl3*$^{-/-}$ and WT mESCs quantified with number of reads mapped to mouse genome divided by reads mapped to m^{6}A modified spike-in using MeRIP-seq data. n = 2 biological replicates. (**D**) The correlation of m^{6}A levels on m^{6}A peak regions between two replicates showed high reproducibility. (**E**) Overlaps of m^{6}A peaks acquired from two replicates showed high reproducibility. (**F**) Scatter plots showing the m^{6}A level of m^{6}A peak regions in WT and *Mettl3* KO mESCs. Hyper-methylated peaks with m^{6}A $\log_2$FC > 1 upon *Mettl3* KO were shown with orange dots, and hypo-methylated peaks with m^{6}A $\log_2$FC < –1 upon *Mettl3* KO were shown with blue dots. (**G**) Distribution of m^{6}A peaks at distinct genomic regions including promoter, TTS, exonic, intronic and intergenic regions annotated by HOMER in WT and *Mettl3* KO mESCs. n = 2 biological replicates. (**H**) Metagene profiles of m^{6}A peak density along transcripts with three non-overlapping segments (5' UTR, CDS, and 3' UTR) for WT and *Mettl3*$^{-/-}$ mESCs.

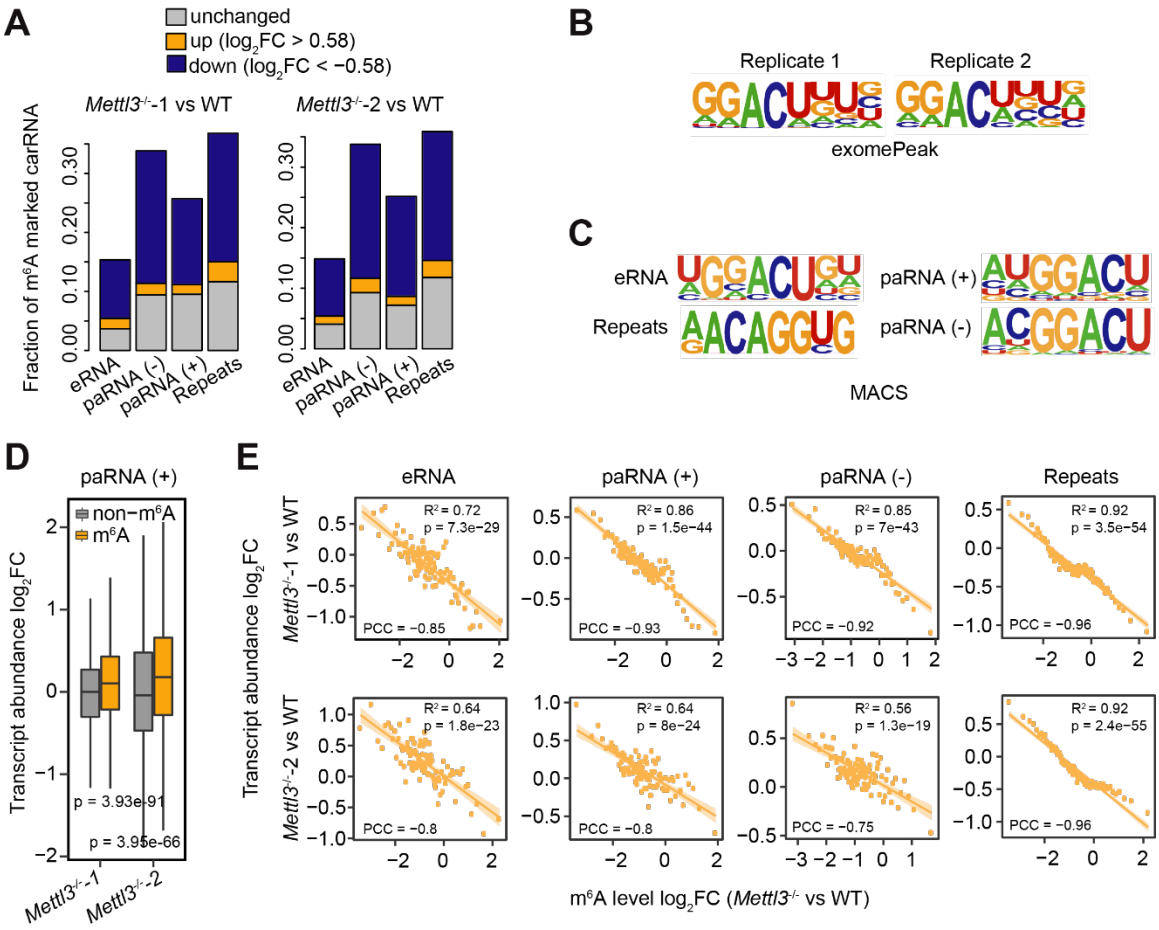

Fig. S3. METTL3 regulates the methylation and abundance of carRNAs. (**A**) Fraction changes of m^{6}A-marked carRNAs upon *Mettl3* KO in mESCs. m^{6}A-marked carRNAs were categorized into up-regulated ($log_2FC > 0.58$), down-regulated ($log_2FC < -0.58$), and unchanged groups according to their m^{6}A level changes upon *Mettl3* KO in mESCs, respectively. (**B-C**) The most enriched consensus motif identified from m^{6}A peaks on exons (B) and carRNAs (C) in WT mESCs. (**D**) Sense paRNAs (paRNA [+]) were divided into methylated (m^{6}A) or non-methylated (non-m^{6}A) groups in mESCs. Boxplot showing greater increases in transcript abundance fold changes of the m^{6}A group versus the non-m^{6}A group upon *Mettl3* KO. *P* values were determined by two-tailed *t* test. (**E**) The negative correlation between changes of m^{6}A level and fold changes of transcript abundance of carRNAs upon *Mettl3* KO. carRNAs within each group were categorized into 100 bins based on their ranked m^{6}A levels fold change upon *Mettl3* KO. R^2 is used to measure the goodness-of-fit for the linear regression model, which indicates the percentage of the dependent variable variation that a linear model explains.

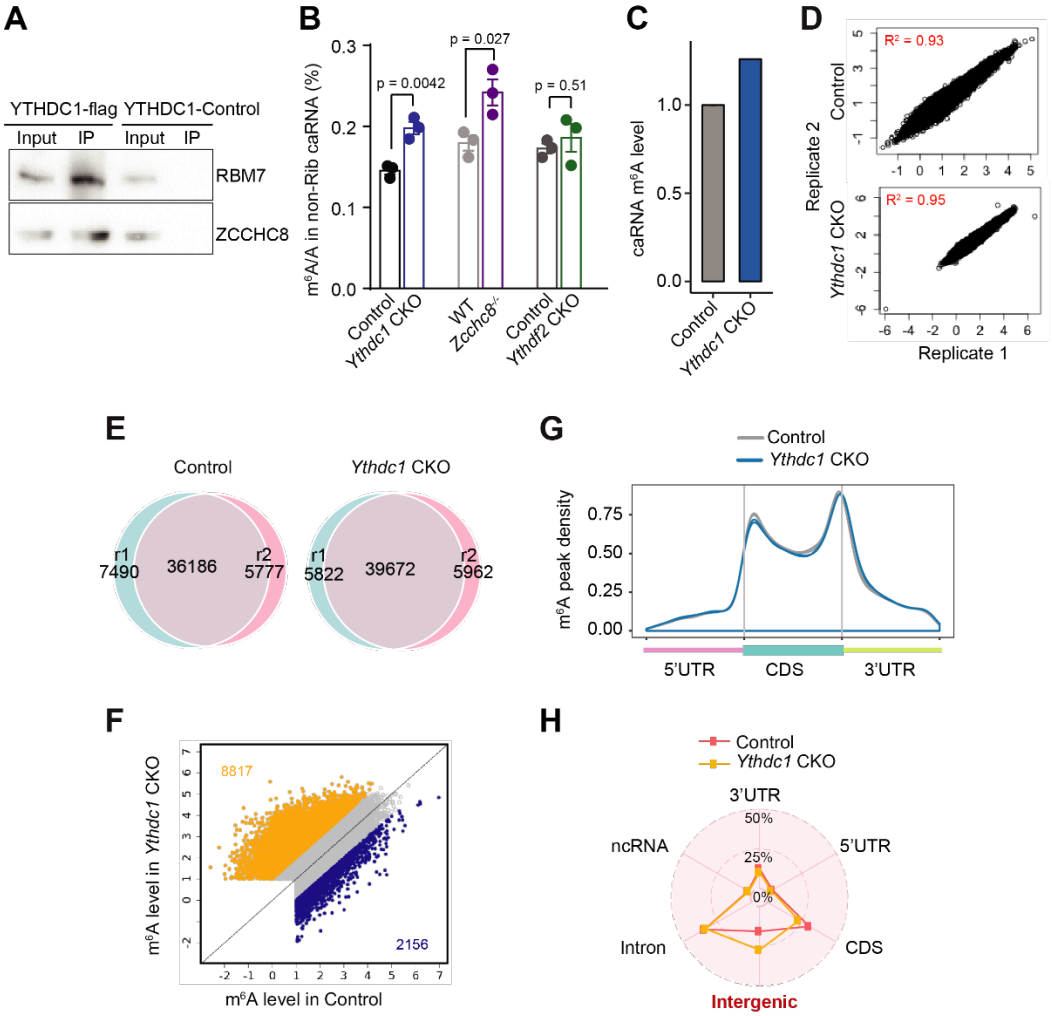

Fig. S4. m^{6}A-seq analysis of caRNAs in *Ythdc1* CKO mESCs. (**A**) Western blots of the immunoprecipitated, FLAG-tagged YTHDC1 from stable expressed mESCs and its interaction with two NEXT complex components. (**B**) LC-MS/MS quantification of the m^{6}A/A ratio in nonribosomal caRNAs in *Ythdc1*, *Zcchc8* and *Ythdf2* depleted mESCs versus their controls, respectively. $n = 3$ biological replicates. Error bars indicate mean ± S.E.M. *P* values were determined by two-tailed *t* test. (**C**) m^{6}A levels of caRNAs in *Ythdc1* CKO and Control mESCs quantified with number of reads mapped to mouse genome divided by reads mapped to m^{6}A-modified spike-in using MeRIP-seq data. $n = 2$ biological replicates. (**D**) The correlation of m^{6}A levels at m^{6}A peak regions between two replicates showed high reproducibility. (**E**) The overlaps of m^{6}A peaks acquired from two replicates showed high reproducibility. (**F**) Scatter plots showing the m^{6}A level at m^{6}A peak regions in Control and *Ythdc1* CKO mESCs. Hyper-methylated peaks with m^{6}A $\log_2$FC > 1 upon *Ythdc1* CKO were shown with orange dots, and hypo-methylated peaks with m^{6}A $\log_2$FC < –1 upon *Ythdc1* CKO were shown with blue dots. (**G**) Metagene profiles of m^{6}A peak density along transcripts with three non-overlapping segments (5' UTR, CDS, and 3' UTR) for Control and *Ythdc1* CKO mESCs. (**H**) Radar chart showing the percentage of m^{6}A peaks on caRNAs distributed at 5' UTR, CDS, 3'UTR, intronic, ncRNA and intergenic regions in the Control and *Ythdc1* CKO mESCs.

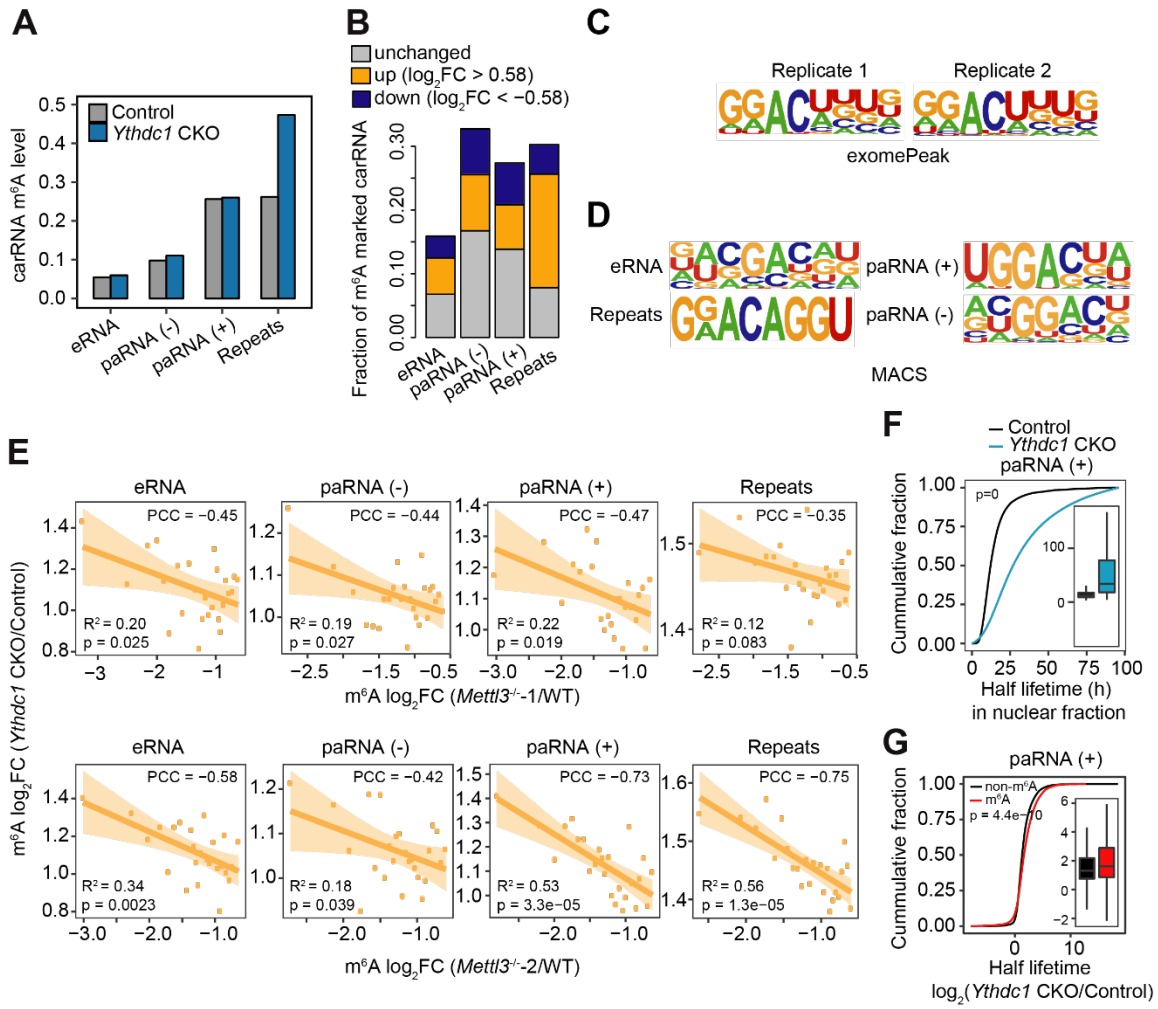

Fig. S5. The m^{6}A level on carRNAs is regulated by *Mettl3* and *Ythdc1*. (**A**) m^{6}A level changes of carRNAs upon *Ythdc1* CKO in mESCs. $n = 2$ biological replicates. (**B**) Fraction changes of m^{6}A-marked carRNAs upon *Ythdc1* CKO in mESCs. m^{6}A-marked carRNAs were categorized into up-regulated ($\log_2$FC > 0.58), down-regulated ($\log_2$FC < –0.58) and unchanged groups according to m^{6}A level changes upon *Ythdc1* CKO in mESCs, respectively. (**C**-**D**) The most enriched consensus motifs identified from m^{6}A peaks on exons (C) and carRNAs (D) in Control mESCs. (**E**) Negative correlations of m^{6}A fold changes of carRNAs between comparing *Mettl3* KO with WT ($\log_2$FC < –0.58) and *Ythdc1* CKO to Control ($\log_2$FC > 0.58). carRNAs within each group were binned into 25 categories according to m^{6}A level fold change ranks upon *Mettl3* KO in mESCs. R^2 is used to measure the goodness-of-fit for the linear regression model, which indicates the percentage of the dependent variable variation that a linear model explains. (**F**) Cumulative distribution and boxplots (inside) of the half lifetime of sense paRNAs in *Ythdc1* CKO and Control mESCs. (**G**) Cumulative distributions and boxplots (inside) of the half lifetime changes of sense paRNAs upon *Ythdc1* CKO. Sense paRNAs were divided into methylated (m^{6}A) or non-methylated (non-m^{6}A) groups. Depletion of YTHDC1 led to greater half lifetime increases of m^{6}A-marked sense paRNAs than non-m^{6}A-marked ones. For (F) and (G), *P* values were calculated by a non-parametric Wilcoxon-Mann-Whitney test.

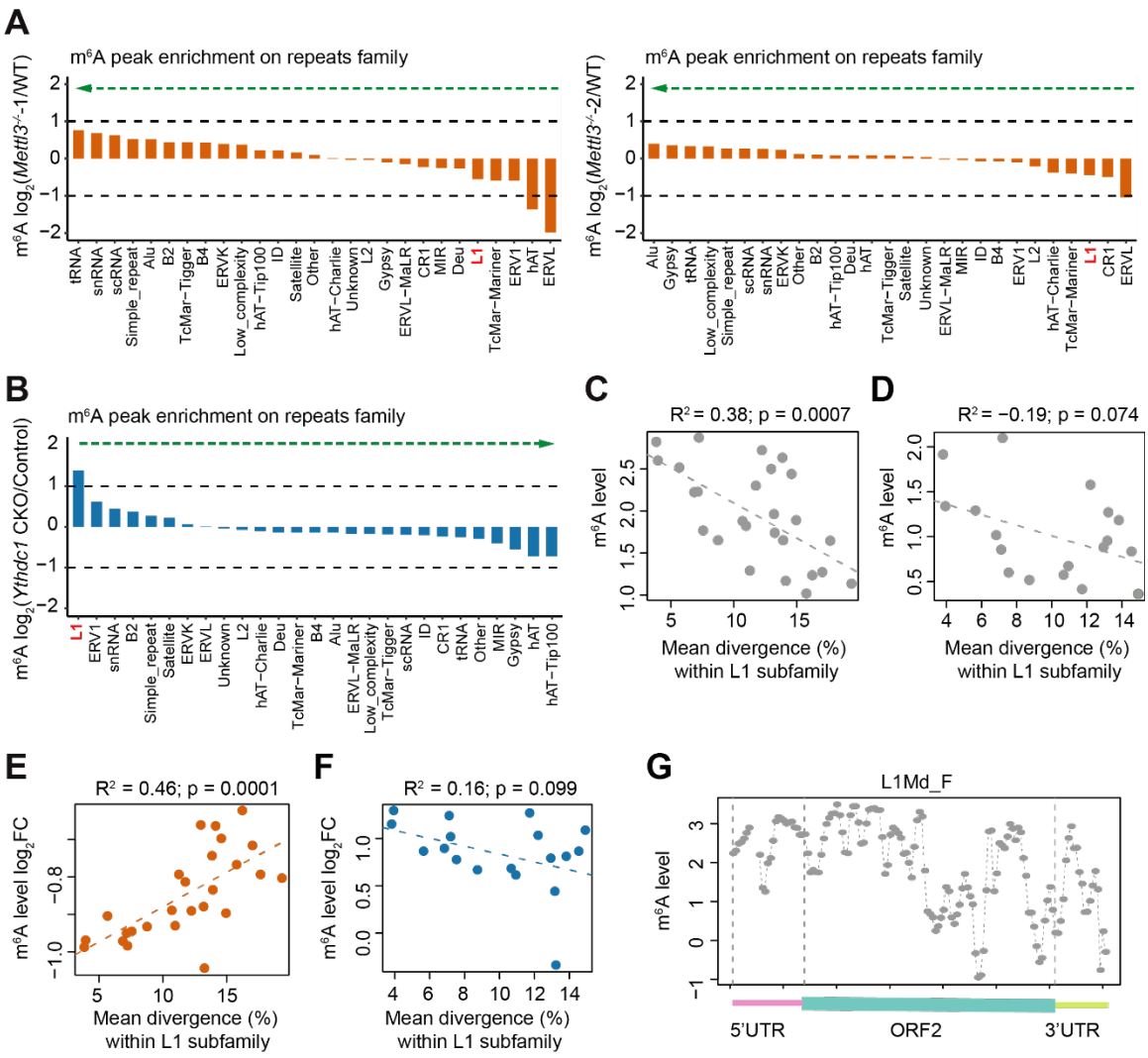

Fig. S6. The m^{6}A level on LINE1 is regulated by *Mettl3* and *Ythdc1*. (**A-B**) Repeats families (x-axis) ranked by m^{6}A peak enrichment fold changes (y-axis) upon *Mettl3* (two biological replicates) (A) or *Ythdc1* (B) depletion versus their controls, respectively. (**C-D**) Scatter plots showing the correlation of the m^{6}A level of L1 subfamilies and their mean divergences in WT (C) or *Ythdc1* Control (D) mESCs. (**E-F**) Scatter plots showing the correlation of the m^{6}A fold changes of L1 subfamilies and their mean divergences upon *Mettl3* (E) or *Ythdc1* (F) depletion versus their controls, respectively. For (C) to (F), L1 subfamilies were ranked by average sequence divergence (<20%) across different elements within each mouse L1 subfamily. (**G**) Metagene profile of the m^{6}A level along consensus sequence of L1Md_F with three segments (5' UTR, ORF2, and 3' UTR) in mESCs.

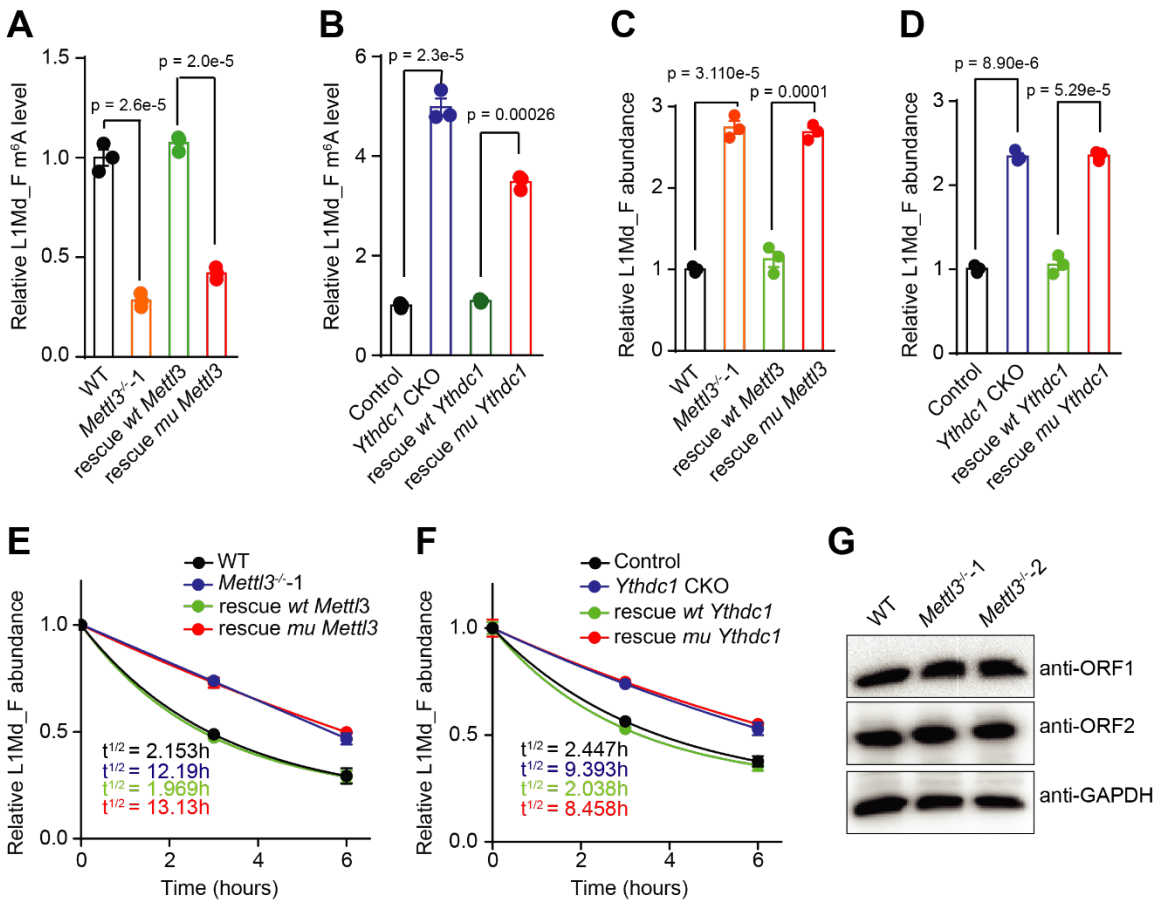

Fig. S7. LINE1 abundance is negatively regulated by *Mettl3* and *Ythdc1* in an m^{6}A-dependent manner. The relative m^{6}A levels (**A** and **B**), expression levels (**C** and **D**) and half lifetimes (**E** and **F**) of L1Md_F quantified with RT-qPCR upon modulating *Mettl3* (A, C, and E) or *Ythdc1* (B, D, and F) in mESCs. $n = 3$ biological replicates. Error bars indicate mean ± S.E.M. *P* values determined by two-tailed *t* test. (**G**) Immunoblots assay showing protein expression levels of ORF1 and ORF2 encoded by LINE1, indicating no obvious changes in WT and *Mettl3* KO mESCs.

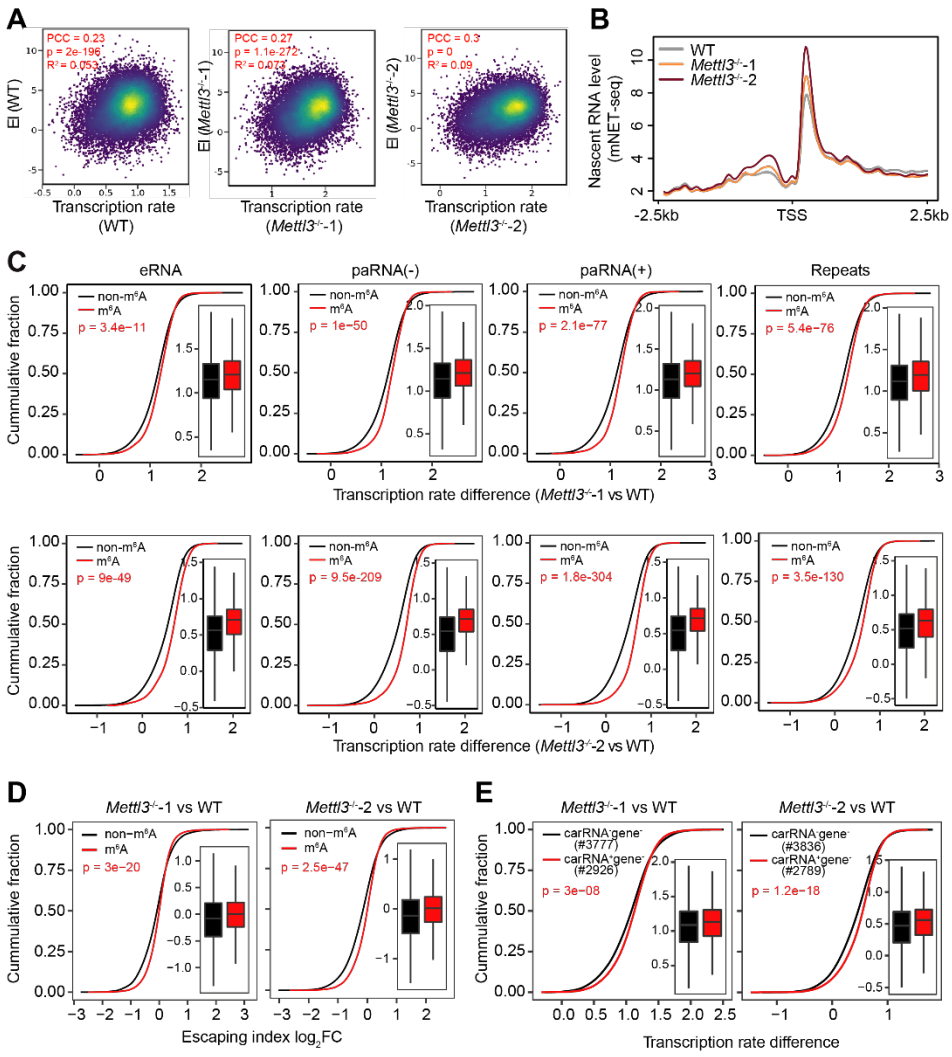

Fig. S8. Increased RNA transcription rate upon *Mettl3* KO. (**A**) Positive correlations were observed between transcription rate and escaping index (EI) in WT and *Mettl3* KO mESCs. R^2 is used to measure the goodness-of-fit for the linear regression model, which indicates the percentage of the dependent variable variation that a linear model explains. (**B**) Profiles of nascent RNA levels at TSS and its flanking 2.5 kb regions quantified through mNET-seq in WT and *Mettl3* KO mESCs. (**C**) Cumulative distributions and boxplots (inside) of gene transcription rate difference between *Mettl3*$^{-/-}$-1 (top) or *Mettl3*$^{-/-}$-2 (bottom) and WT mESCs. Genes were categorized into two subgroups (m^{6}A and non-m^{6}A) according to whether they are regulated by m^{6}A-marked carRNAs (m^{6}A) or not (non-m^{6}A). (**D**) Cumulative distributions and boxplots (inside) of $\log_2$FC (fold changes) of gene escaping index normalized with quantile. Genes were categorized into two groups according to whether they harbor upstream m^{6}A-marked carRNA (m^{6}A) or not (non-m^{6}A). (**E**) Cumulative distributions and boxplots (inside) of gene transcription rate difference upon *Mettl3* KO in mESCs. Genes whose pre-mRNA are not subject to m^{6}A methylation were categorized into two subgroups according to whether they harbor m^{6}A-marked upstream carRNAs (carRNA$^+$gene$^-$) or not (carRNA$^-$gene$^-$). For (C) to (E), *P* values were calculated by a non-parametric Wilcoxon-Mann-Whitney test.

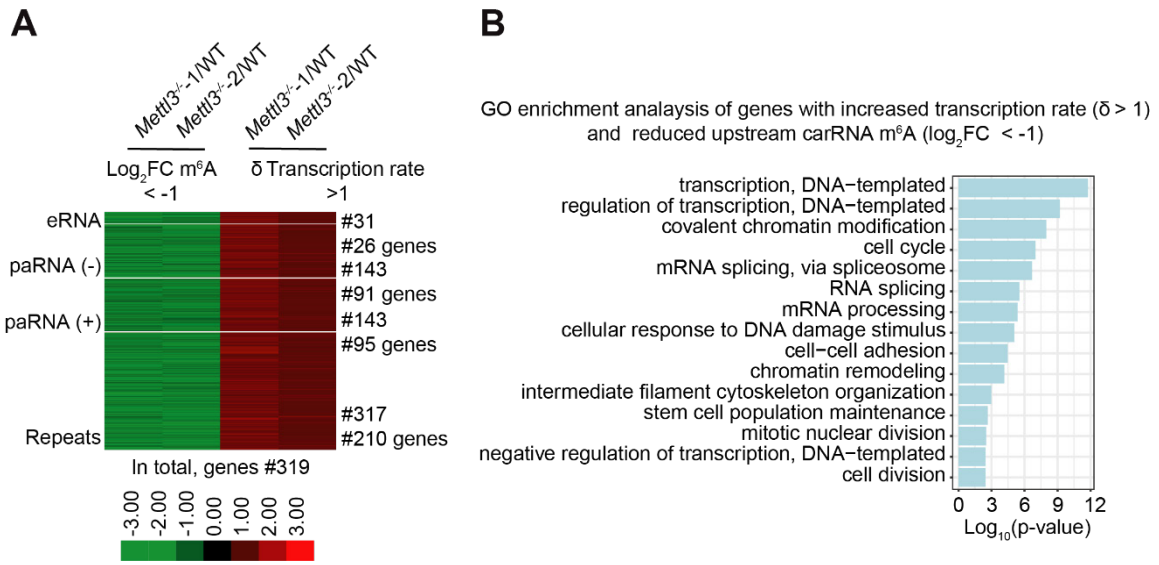

Fig. S9. Function analyses of genes with increased transcription rate and decreased m^{6}A level of their upstream carRNAs upon *Mettl3* KO. (**A**) Heatmap showing m^{6}A level fold changes ($log_2FC < -1$) on carRNAs and downstream gene transcription rate difference ($\delta > 1$) between *Mettl3* KO and WT mESCs. (**B**) Gene Ontology (GO) enrichment analysis of genes in (A).

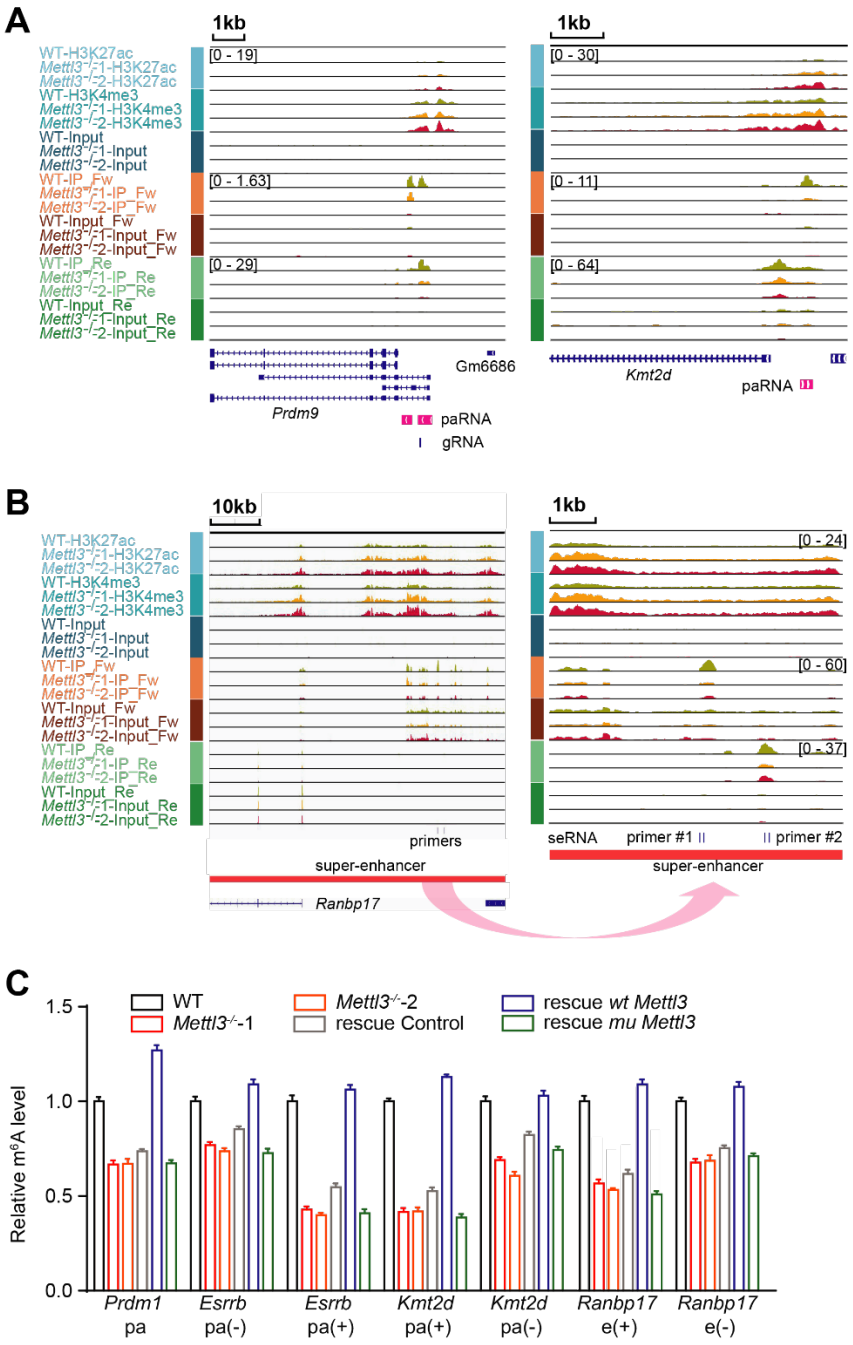

Fig. S10. The m^{6}A level decreased in carRNAs upon *Mettl3* KO. (**A-B**) IGV profiles showing increased H3K27ac and H3K4me3 modification levels and decreased m^{6}A level at paRNA regions of *Prdm9* and *Kmt2d* (A) and seRNA region of *Ranbp17* (B) in *Mettl3*$^{-/-}$ mESCs versus wild type. Profiles of m^{6}A RNA were separated into forward (Fw) and reverse (Re) strands according to the strand they were mapped to, gRNA targeting paRNA of *Prdm9* and the primers for the seRNA of *Randb17* were labeled as one track. (C) The relative m^{6}A level of carRNAs for specific genes were quantified with m^{6}A-IP followed by RT-qPCR in *Mettl3*$^{-/-}$ mESCs versus wild type, and rescued with *wt Mettl3* versus *mu Mettl3* mESCs. n = 3 biological replicates. Error bars indicate mean ± S.E.M.

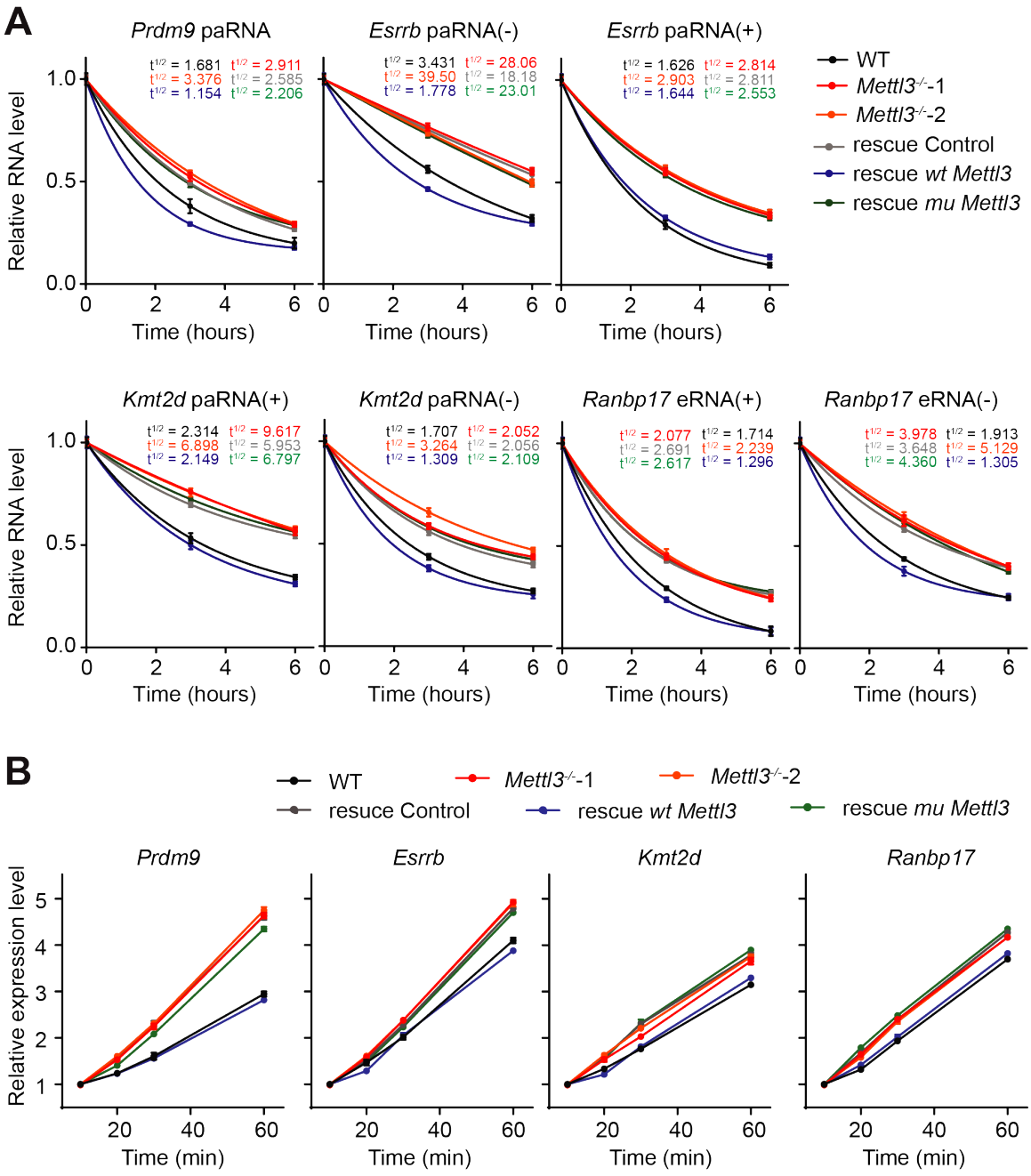

Fig. S11. METTL3 modulates the decay of carRNAs and the transcription of downstream genes in an m^{6}A-dependent manner. Half lifetime of carRNAs (**A**) and transcription rates of downstream genes (**B**) in WT, *Mettl3*$^{-/-}$, rescued with *wt Mettl3* or *mu Mettl3* mESCs and quantified by RT-qPCR. $n = 3$ biological replicates. Error bars indicate mean ± S.E.M.

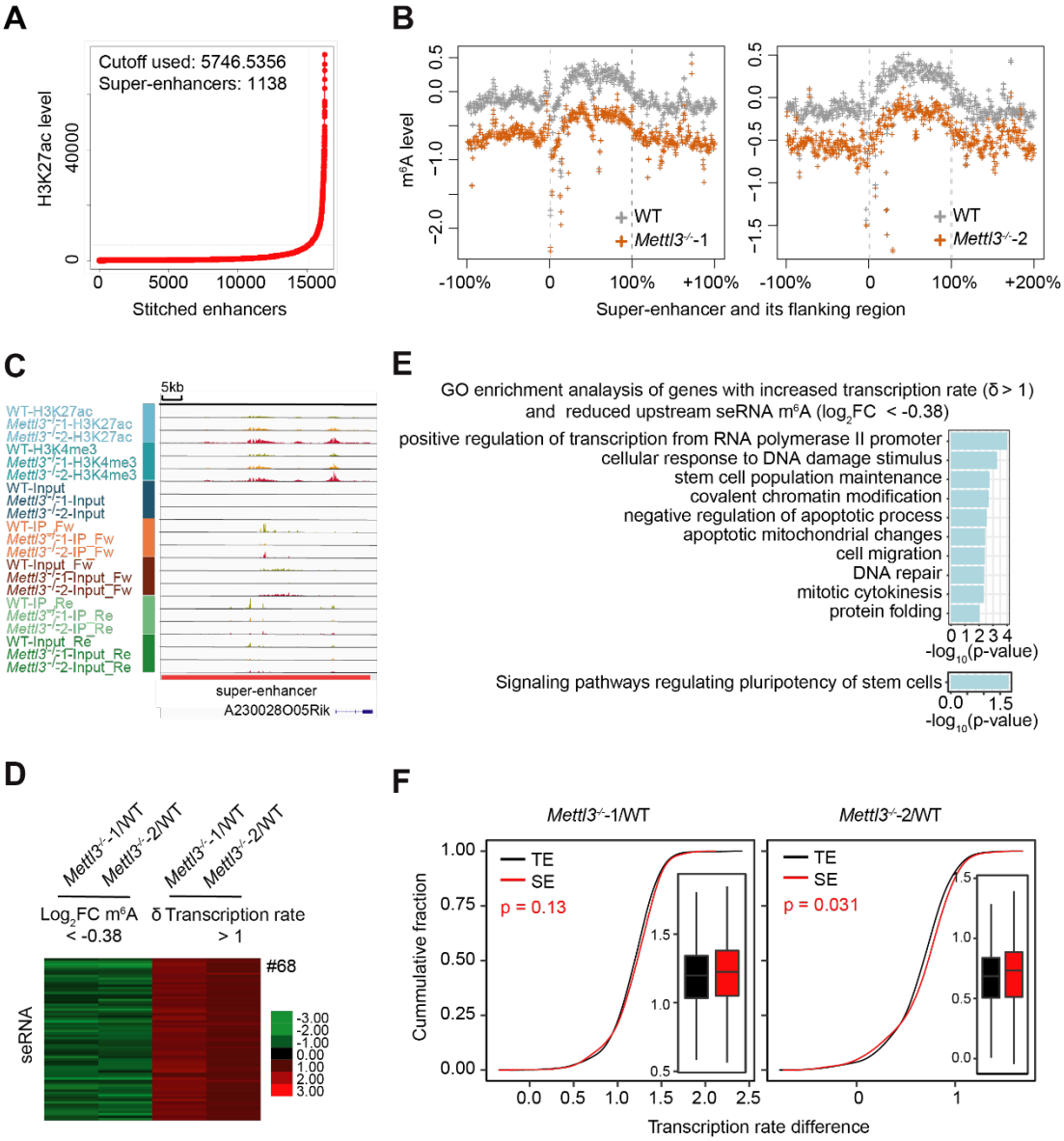

Fig. S12. m^{6}A on super-enhancer RNA (seRNA) is regulated by METTL3. (**A**) Super-enhancers in WT mESCs identified by ROSE using H3K27ac ChIP-seq data. (**B**) Profiles of m^{6}A level on seRNAs and their flanking regions in WT and *Mettl3*$^{-/-}$ mESCs. (**C**) IGV profiles showing increased H3K27ac and H3K4me3 modification levels, and decreased m^{6}A level in seRNAs between *Mettl3*$^{-/-}$ and WT mESCs. Profiles of m^{6}A RNA were separated into forward (Fw) and reverse (Re) strands according to the strand they mapped to. (**D**) Heatmap showing the fold changes ($\log_2$FC < –0.38) of m^{6}A level of seRNAs and changes ($\delta > 1$) of downstream gene transcription rate between *Mettl3* KO and WT mESCs. (**E**) Gene Ontology (GO) enrichment analysis of genes in (D). (**F**) Cumulative distributions and boxplots (inside) of gene transcription rate difference upon *Mettl3* KO in mESCs. Genes were categorized into two groups according to whether they harbor m^{6}A-marked upstream typical eRNA (TE) or seRNA (SE). *P* values were calculated by a non-parametric Wilcoxon-Mann-Whitney test.

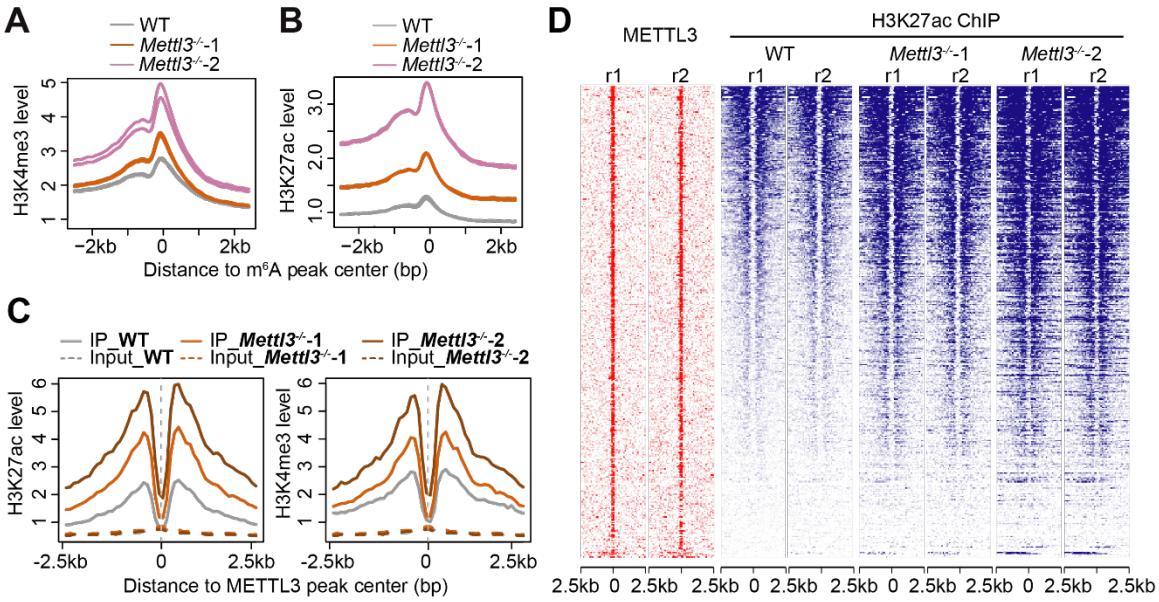

Fig. S13. m^{6}A on carRNAs affects chromatin state. (**A** and **B**) Profiles of H3K4me3 (A) and H3K27ac (B) levels at the center of m^{6}A peaks and its flanking 2.5 kb in WT and *Mettl3*$^{-/-}$ mESCs. (**C**) Profiles of H3K27ac (left) and H3K4me3 (right) levels on the center of DNA loci bound by METTL3 and its flanking 2.5 kb in WT and *Mettl3*$^{-/-}$ mESCs. (**D**) Heatmap showing H3K27ac level in WT and *Mettl3*$^{-/-}$ mESCs around the METTL3-bound DNA loci (within 2.5 kb range).

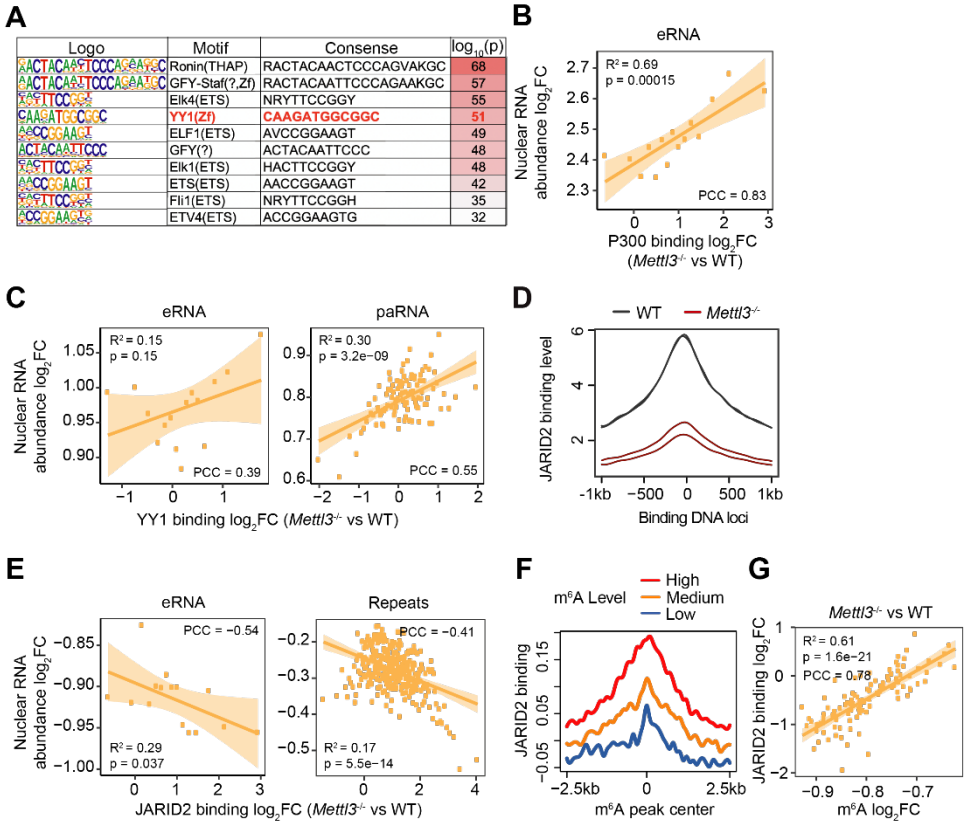

Fig. S14. m^{6}A on carRNAs regulates chromatin state through affecting transcription factor binding. (**A**) TF motif enrichment analysis at genomic regions with m^{6}A-marked paRNAs using HOMER. (**B**) The correlation between the change in EP300 binding at m^{6}A-containing eRNA regions and changes in eRNA abundance upon *Mettl3* KO in mESCs. Every 100 eRNAs, ranked by fold change of EP300 binding upon *Mettl3* KO, were grouped and averaged as one data point. (**C**) The correlation between changes in YY1 binding at m^{6}A-containing eRNA/paRNA regions and changes in abundances of eRNA/paRNA upon *Mettl3* KO in mESCs. Every 100 eRNAs or paRNAs, ranked by fold change of YY1 binding upon *Mettl3* KO were grouped and averaged as one data point. (**D**) Profiles of JARID2 DNA binding at the peak center and flanking 2.5 kb regions in WT and *Mettl3* KO mESCs. (**E**) The correlation between changes in JARID2 binding at m^{6}A-containing eRNA or repeats regions and changes in abundance of eRNAs/repeat RNAs upon *Mettl3* KO in mESCs. Every 100 eRNAs or repeats, ranked by fold changes of JARID2 binding upon *Mettl3* KO, were grouped and averaged as one data point. (**F**) Profiles of JARID2 binding at the center of m^{6}A peaks overlapped with carRNAs and its flanking 2.5 kb regions in WT mESCs. m^{6}A peaks were categorized into highly (high), moderately (medium) or lowly (low) methylated groups according to their m^{6}A levels in WT mESCs. (**G**) The correlation between changes in m^{6}A level and changes in JARID2 binding at genomic regions that contain m^{6}A-marked carRNAs upon *Mettl3* KO. The genomic regions were categorized into 100 bins based on fold change rank of m^{6}A level upon *Mettl3* KO. For (B), (C), (E), and (G), R^2 is used to measure the goodness-of-fit for the linear regression model, which indicates the percentage of the dependent variable variation that a linear model explains.

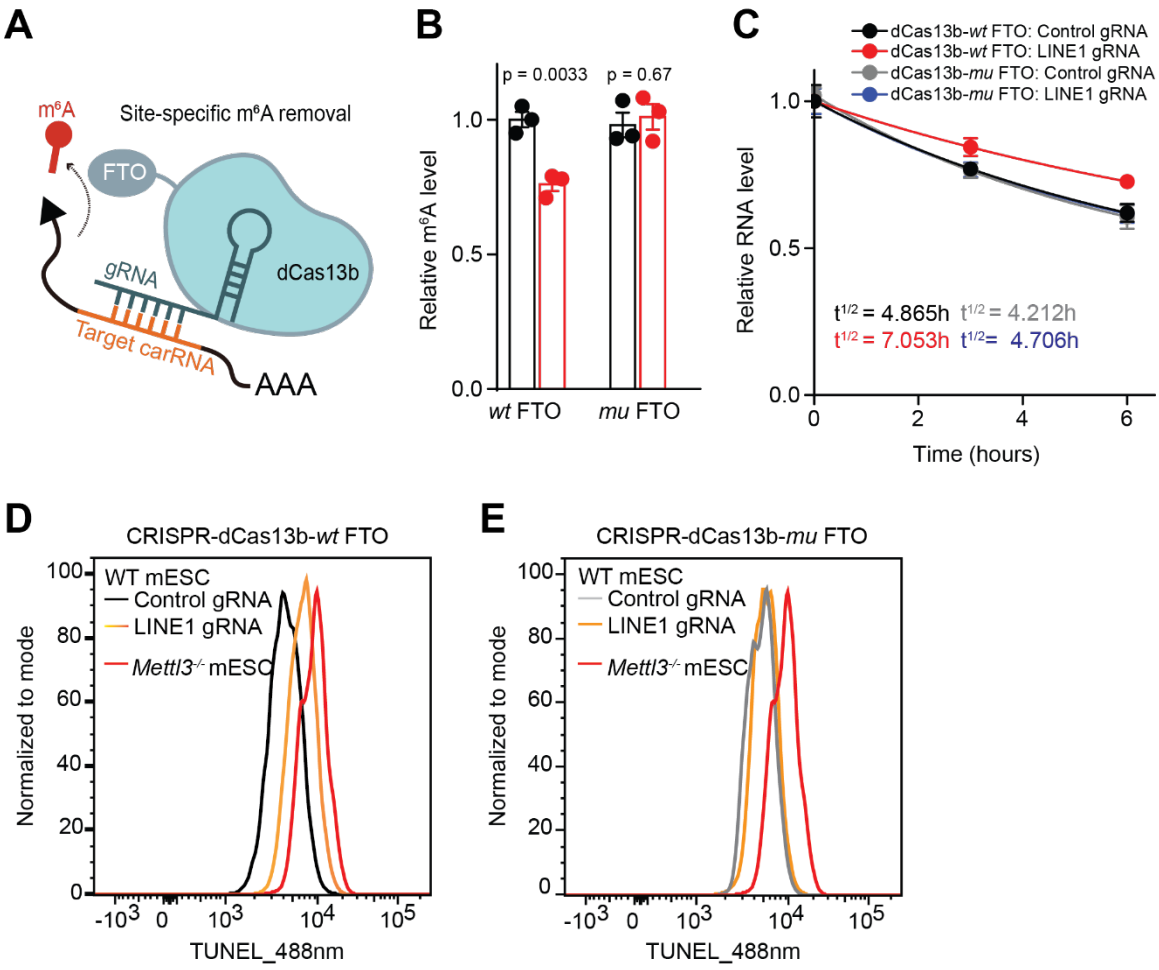

Fig. S15. LINE1 affects chromatin accessibility in WT and *Mettl3* KO mESCs in a methylation-dependent manner. (**A**) A schematic model showing the dCas13b-FTO site-specific demethylation system. (**B to E**) A dCas13b-FTO (wild-type or inactive mutant) construct with gRNA targeting m^{6}A-marked LINE1 was applied to modulate the m^{6}A methylation level of LINE1 (B), which led to changes in half lifetime of LINE1 (C) and global chromatin accessibility (D and E).

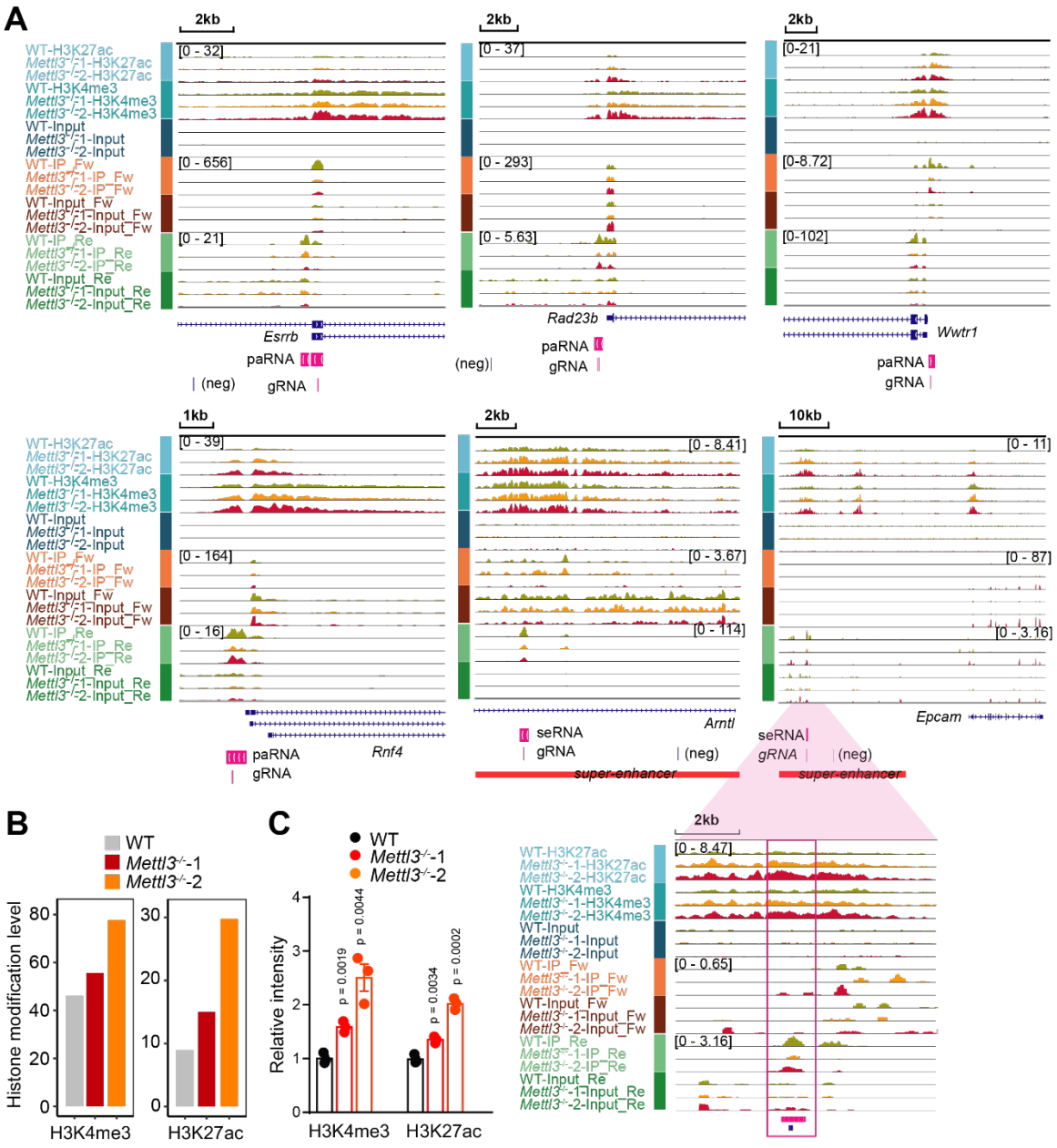

Fig. S16. IGV profiles showing methylation peaks and local histone modifications of carRNAs of selected genes. (**A**) IGV profiles showing increased H3K27ac and H3K4me3 modification levels and decreased m^{6}A level at carRNA regions of *Rad23b, Wwtr1, Prdm9, Rnf4, Arntl* and *Epcam* in *Mettl3*$^{-/-}$ mESCs versus wild type. Profiles of m^{6}A RNA were separated into forward (Fw) and reverse (Re) strands according to the strand they were mapped to, gRNA targeting these carRNAs and their respective distal negative gRNAs (neg) were labeled as one track. (**B and C**) Quantification of histone mark changes at the promoter region of *Esrrb* in WT and *Mettl3* KO mESCs as a representative with both ChIP-seq (B, n = 2 biological replicates) and ChIP-qPCR (C, n = 3 biological replicates). Error bars indicate mean ± S.E.M.

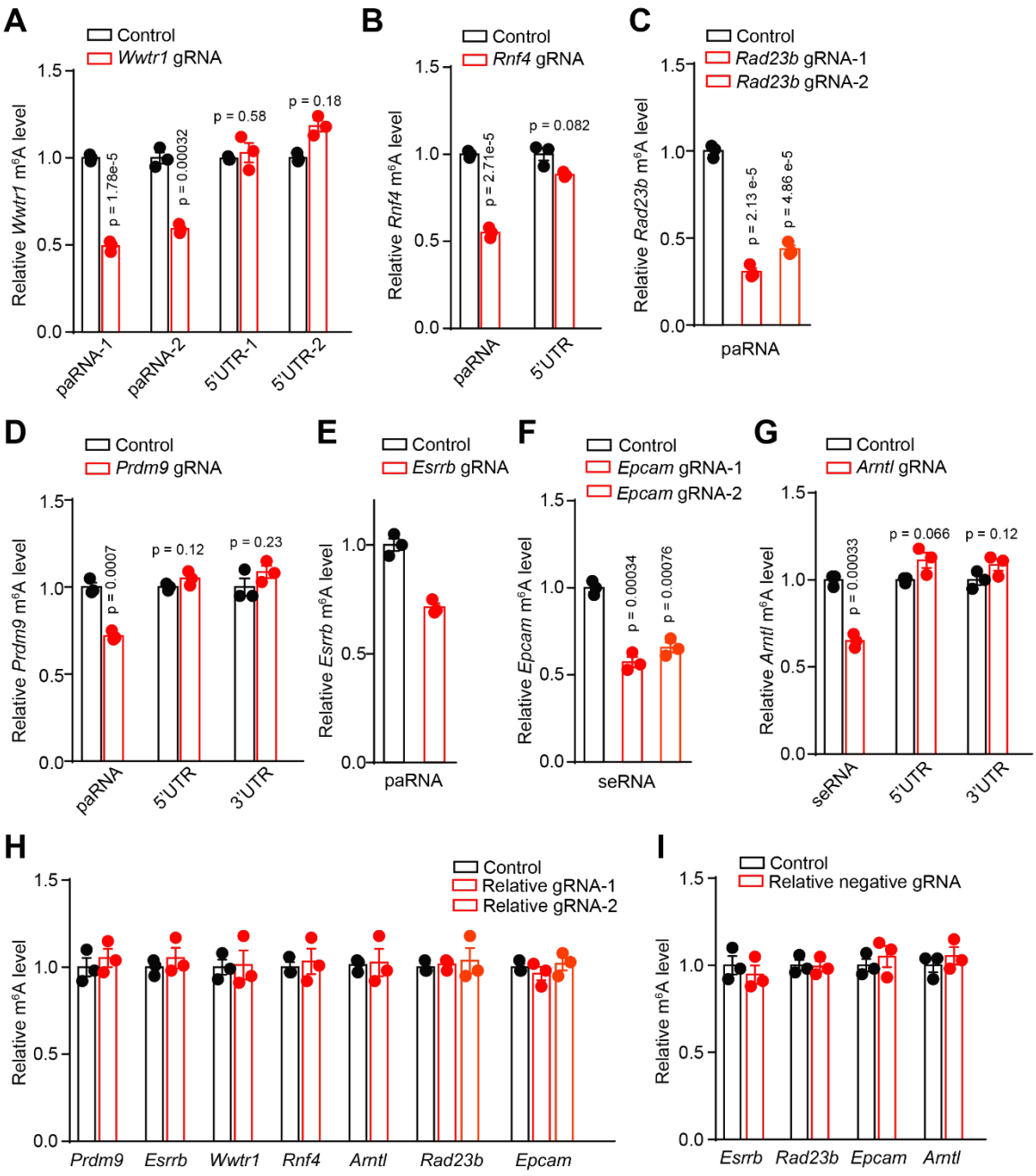

Fig. S17. carRNA methylation level changes applying dCas13b-FTO. (**A-G**) A dCas13b-*wt* FTO construct with gRNAs targeting the carRNA regions of *Wwtr1*(A), *Rnf4* (B), *Rad23b* (C), *Prdm9* (D), *Esrrb* (E), *Epcam* (F) and *Arntl* (G), respectively, was used to reduce the m^{6}A level of these corresponding carRNAs. (**H**) A dCas13b-*mu* FTO (inactive FTO) construct with gRNAs targeting the carRNA regions of *Wwtr1*, *Rnf4*, *Rad23b*, *Prdm9*, *Esrrb, Epcam* and *Arntl*, respectively, didn't result in notable changes in the m^{6}A level. (**I**) A dCas13b-*wt* FTO construct with negative guide RNAs (ngRNAs) targeting the same loci but outside the carRNA region of *Esrrb*, *Rad23b*, *Epcam* and *Arntl*, respectively. $n = 3$ biological replicates, error bars indicate mean ± S.E.M.

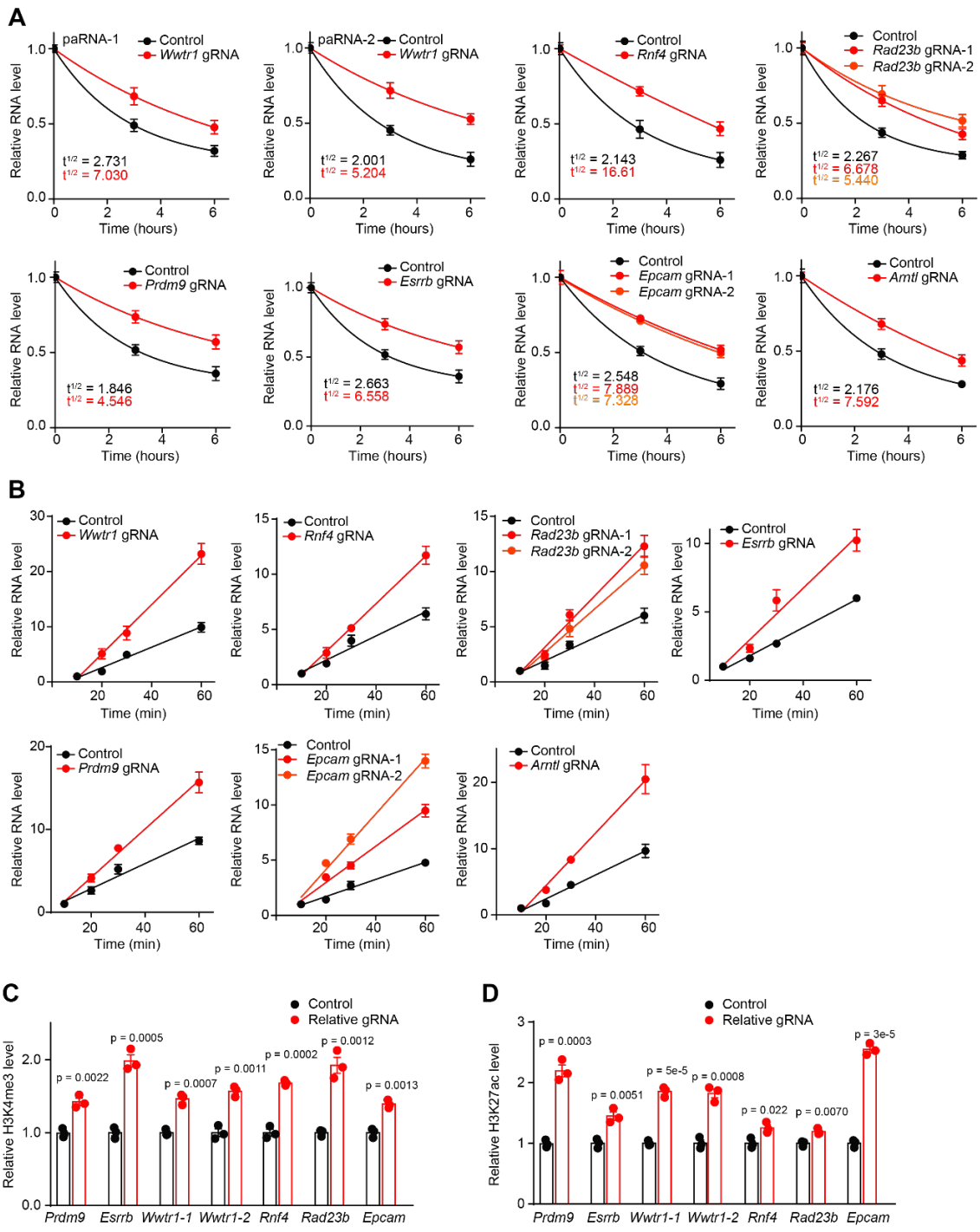

Fig. S18. **Changes of the half lifetime of carRNAs and the downstream gene transcription rate applying dCas13b-FTO.** (**A-D**) A dCas13b-*wt* FTO construct with gRNAs targeting the carRNA regions of *Wwtr1*, *Rnf4*, *Rad23b*, *Prdm9*, *Esrrb, Epcam* and *Arntl*, respectively, led to increased half lifetime of the carRNAs (A), higher transcription rate of the corresponding downstream genes (B), and elevated local active histone marks (C and D). n = 3 biological replicates, error bars indicate mean ± S.E.M. P values were determined by two-tailed t test.

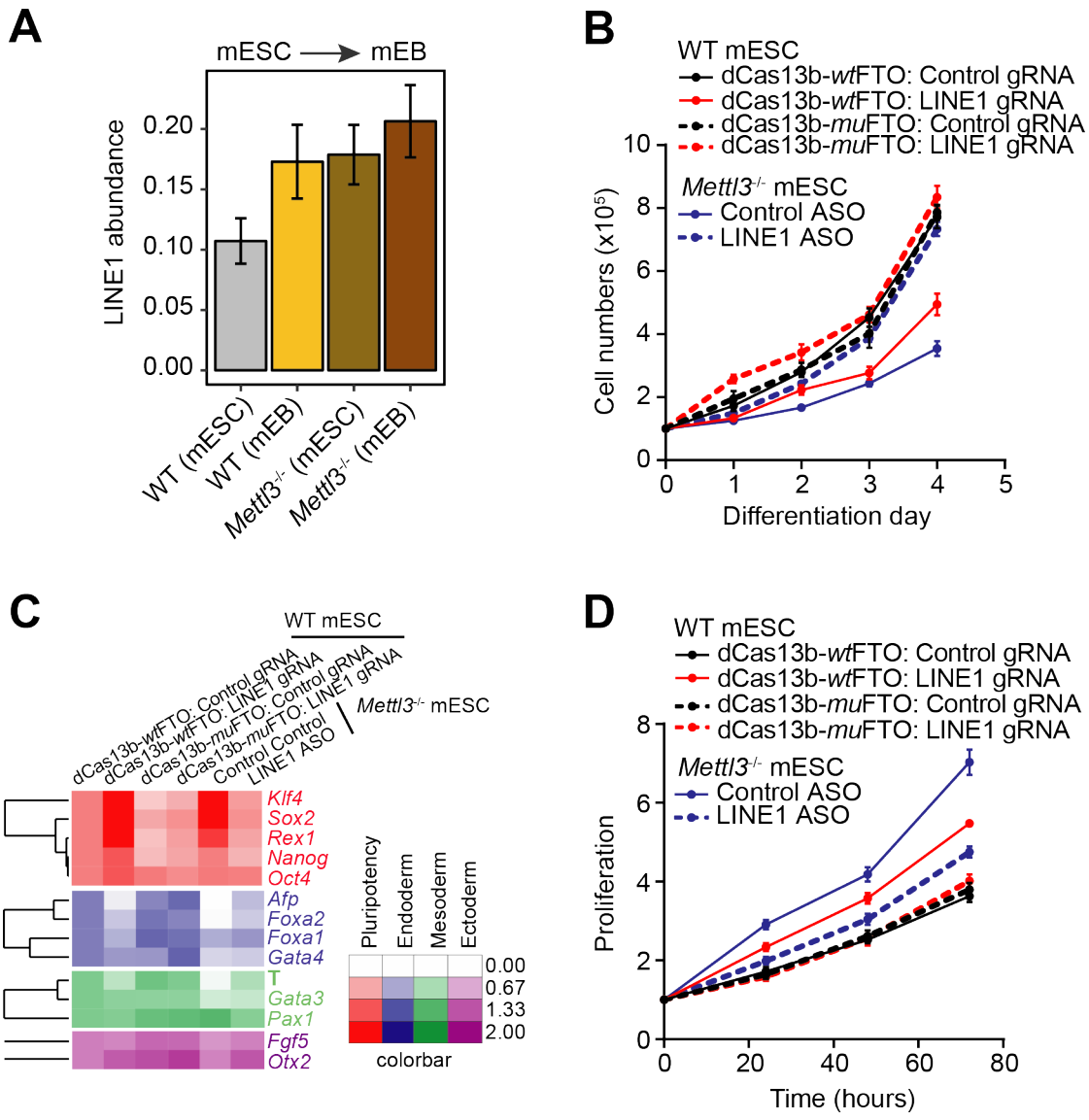

Fig. S19. LINE1 affects stem cell differentiation and proliferation in an m^{6}A-dependent manner. (**A**) LINE1 abundance in WT and *Mettl3* KO mESCs and embryonic body (mEB) (GSE61997) (*11*). Error bars indicate mean ± S.E.M. (**B-D**) Analysis of mEB formation capacity (B), expression of differentiation genes (C) and mESCs proliferation (D) upon LINE1 knockdown in *Mettl3* KO mESCs or when LINE1 is targeted using a gRNA with dCas13b-FTO (wild-type or inactive mutant) in WT mESCs.

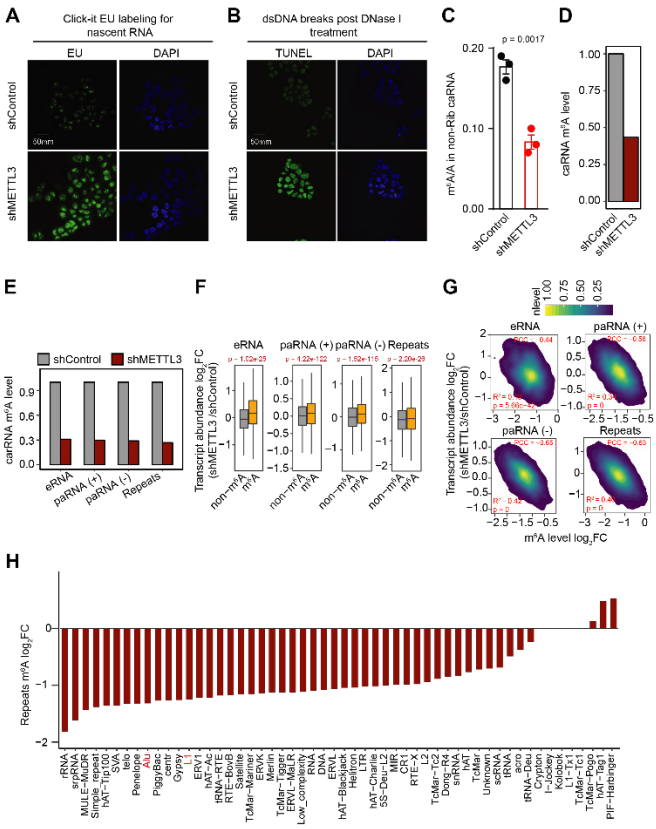

Fig. S20. *METTL3* knockdown affects nascent RNA transcription, chromatin openness, carRNA methylation and carRNA abundance in HEC-1-A cells. (**A**) Analysis of nascent RNA synthesis in the control and *METTL3* knockdown HEC-1-A cells with a click-it RNA Alexa fluor 488 imaging kit. (**B**) Analysis of chromatin accessibility in control and *METTL3* knockdown HEC-1-A cells with DNase I-treated TUNEL assay. For (A) and (B), nucleus is counterstained by DAPI. (**C**) LC-MS/MS quantification of the m^6A/A ratio in nonribosomal, chromosome-associated RNAs extracted from control and *METTL3* knockdown HEC-1-A cells, n = 3 biological replicates. Error bars indicate mean ± S.E.M. *P* values were determined by two-tailed *t* test. (**D**) m^6A levels of caRNAs in control and *METTL3* knockdown HEC-1-A cells quantified with number of reads mapped to human genome divided by reads mapped to m^6A modified spike-in using MeRIP-seq data. (**E**) m^6A level changes for different groups of carRNAs quantified by normalizing m^6A-seq results with spike-in between control and *METTL3* knockdown HEC-1-A cells. For (D) and (E), *n* = 2 biological replicates. (**F**) carRNAs were divided into methylated (m^6A) or non-methylated (non-m^6A) groups in HEC-1-A cells. Boxplots showing greater increases in transcript abundance fold changes of the m^6A group versus the non-m^6A group upon *METTL3* knockdown over the control HEC-1-A cells. *P* values were calculated by two-sided *t* test. (**G**) Negative correlations were observed between the fold changes of m^6A level and the fold changes of transcript abundance upon *METTL3* knockdown in HEC-1-A cells. R^2 is used to measure the goodness-of-fit for the linear regression model, which indicates the percentage of the dependent variable variation that a linear model explains. (**H**) Fold changes of m^6A level of repeat subfamilies between control and *METTL3* knockdown HEC-1-A cells. *n* = 2 biological replicates.

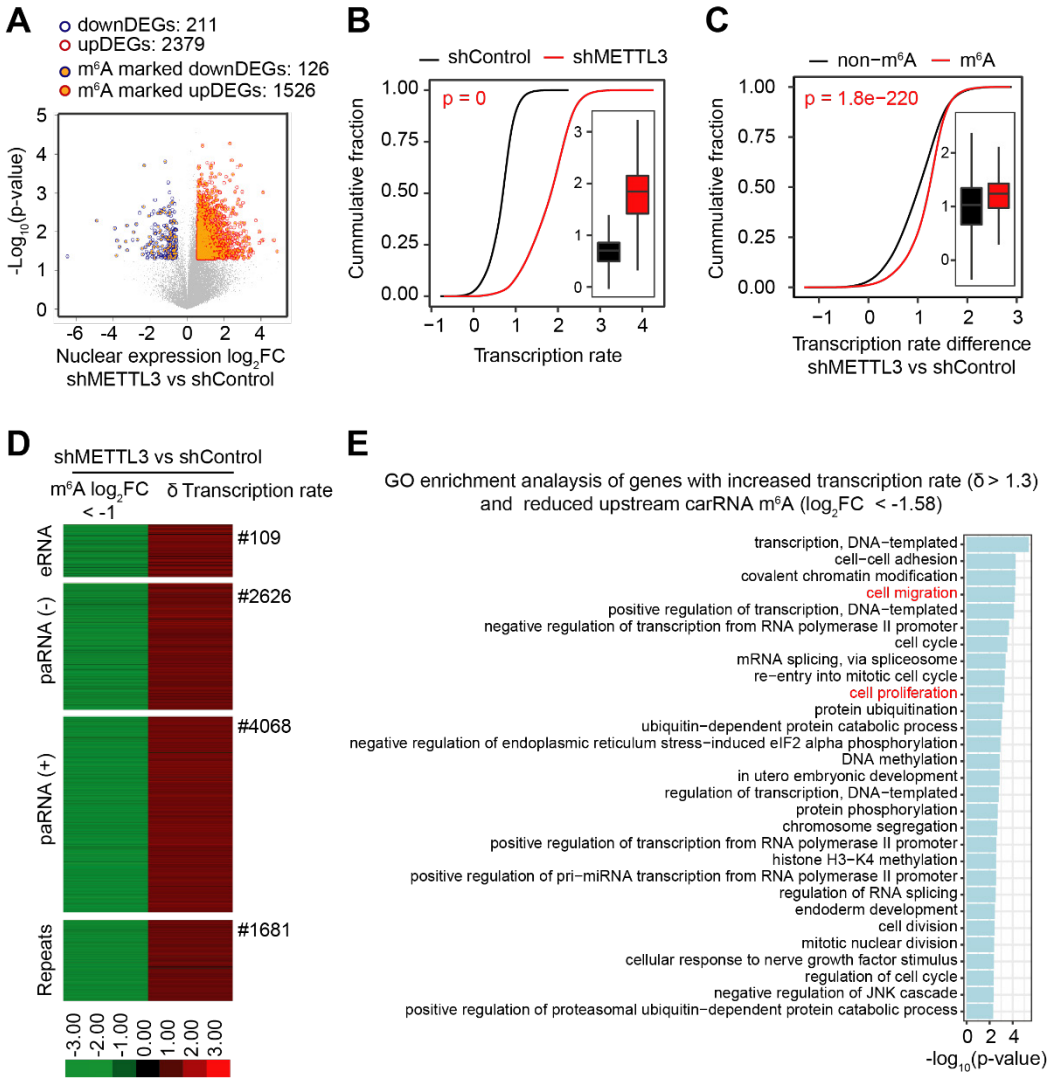

Fig. S21. The m^{6}A level of carRNA affects downstream gene expression and transcription rate. (**A**) Volcano plot of genes with differential expression levels in *METTL3* knockdown versus control HEC-1-A cells (P value < 0.05 and $|\log_2 FC| > 1$). Genes with upstream, m^{6}A-marked carRNAs were showed with orange circles. Gene expression level was normalized to ERCC spike-in with linear regression method. *P* values were calculated by two-sided *t* test. (**B**) Cumulative distribution and boxplot (inside) of transcription rate in control and *METTL3* knockdown HEC-1-A cells. (**C**) Cumulative distribution and boxplot (inside) of gene transcription rate difference upon *METTL3* knockdown in HEC-1-A cells. Genes were categorized into two groups according to whether they harbor m^{6}A-marked upstream carRNAs (m^{6}A) or not (non-m^{6}A). For (B) and (C), *P* values were calculated by a non-parametric Wilcoxon-Mann-Whitney test. (**D**) Heatmap showing the m^{6}A level fold-changes ($\log_2 FC < -1$) on carRNAs and the transcription rate difference of downstream genes between *METTL3* knockdown and control HEC-1-A cells. (**E**) Gene Ontology (GO) enrichment analysis of genes with increased transcription rate ($\delta > 1.3$) and their reduced upstream carRNA m^{6}A level ($\log_2 FC < -1.58$) between *METTL3* knockdown and control HEC-1-A cells.

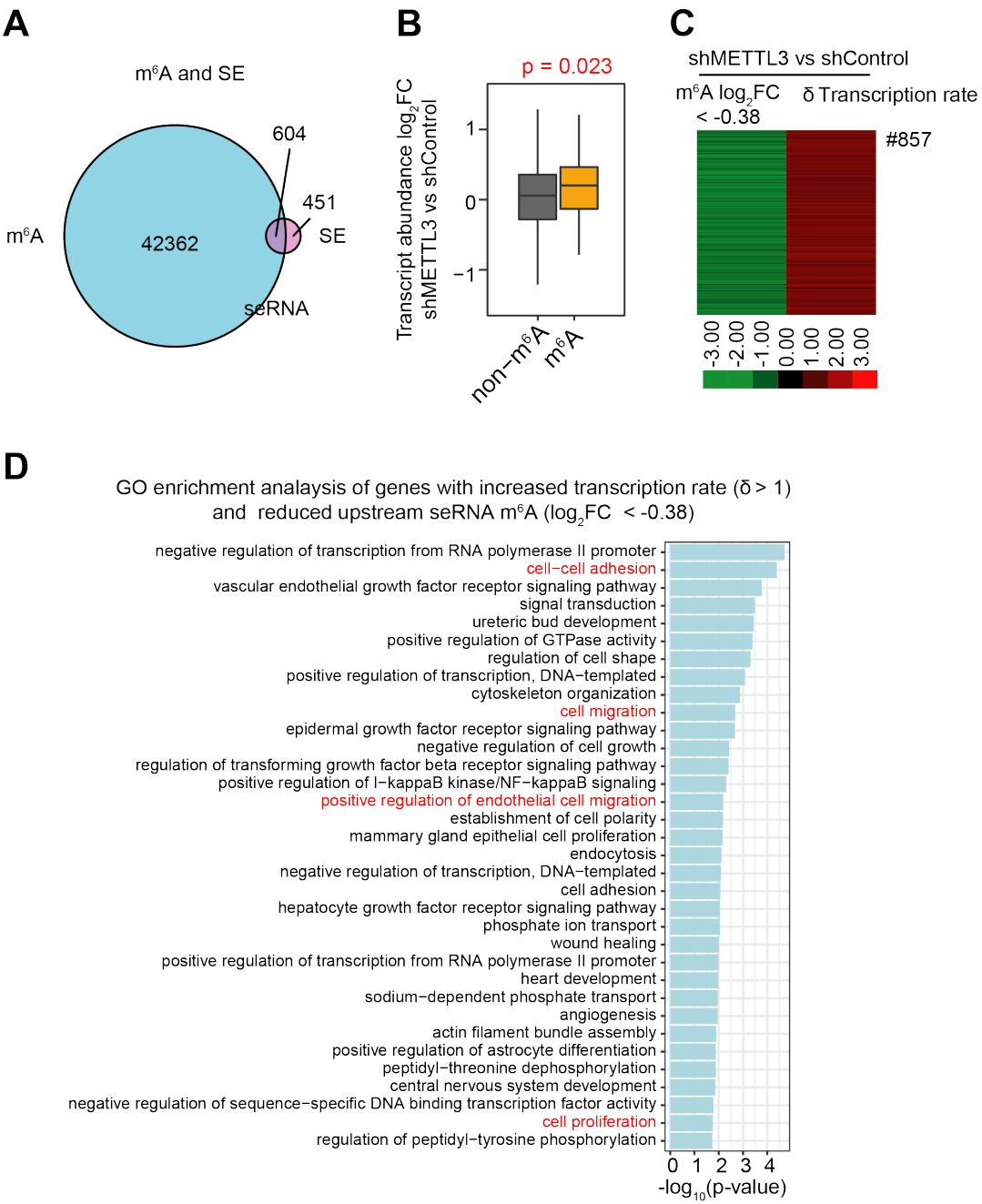

Fig. S22. The m^{6}A level of seRNA affects downstream gene transcription rate in HEC-1-A cells. (**A**) Venn diagram showing the overlap between the m^{6}A peaks and super-enhancer peaks in HEC-1-A cells. (**B**) Boxplot showing fold changes of the abundance of m^{6}A-marked and non-m^{6}A-marked seRNA transcripts between *METTL3* knockdown and control HEC-1-A cells. *P* value was determined by two-tailed *t* test. (**C**) Heatmap showing fold change ($log_2FC < –0.38$) of m^{6}A level of seRNAs and transcription rate difference of their downstream genes between *METTL3* knockdown and control HEC-1-A cells. (**D**) Gene Ontology (GO) enrichment analysis of genes with increased transcription rate ($\delta > 1$) and reduced upstream seRNA m^{6}A level ($log_2FC < –0.38$) between *METTL3* knockdown and control HEC-1-A cells.

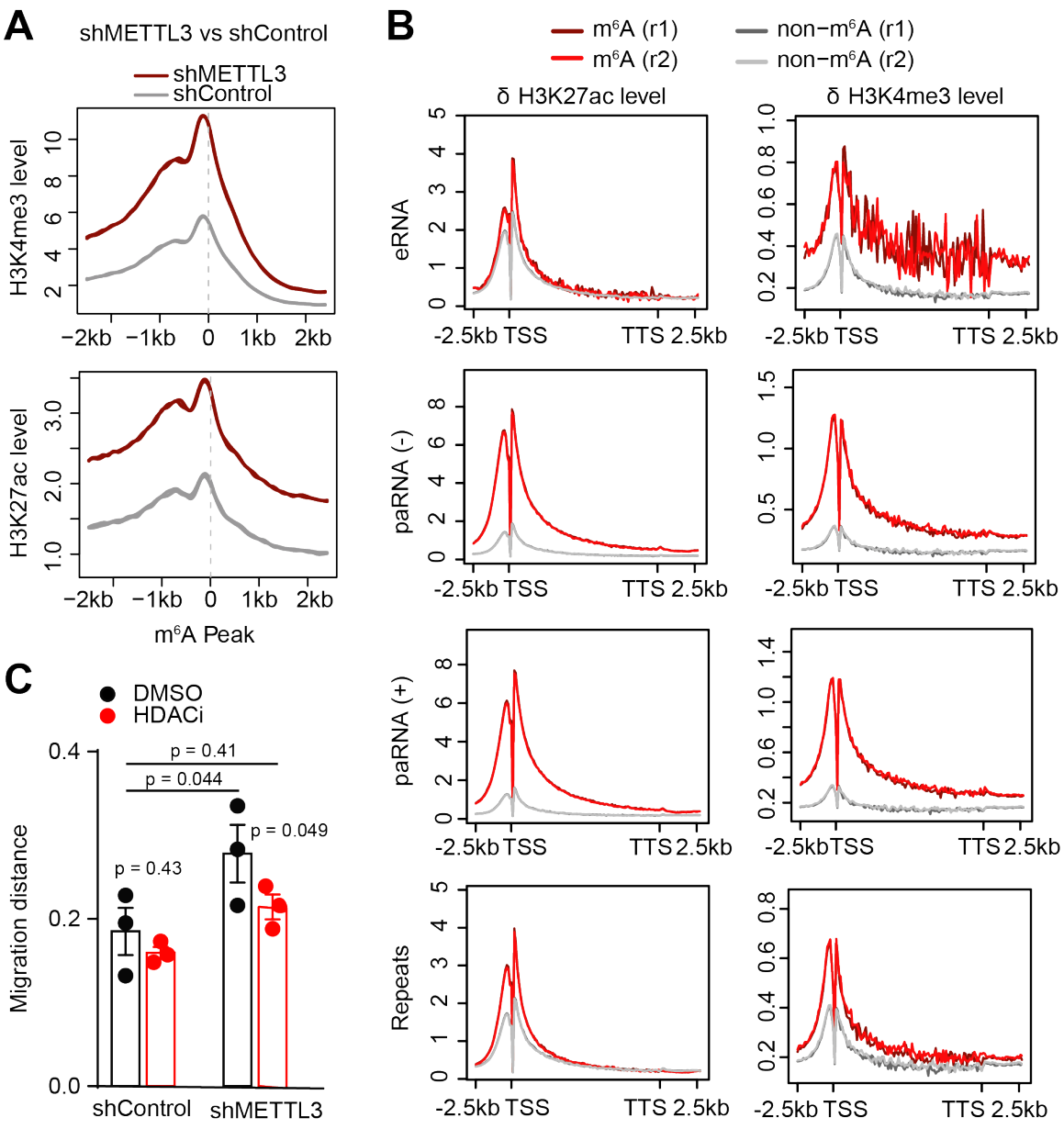

Fig. S23. The m^{6}A level of carRNAs affects local chromatin state. (**A**) Profiles of H3K4me3 and H3K27ac modification levels at m^{6}A peak center and their flanking 2.5 kb regions in control and *METTL3* knockdown HEC-1-A cells. (**B**) Profiles of H3K27ac and H3K4me3 modification level changes in *METTL3* knockdown versus control HEC-1-A cells at the gene bodies, upstream 2.5 kb regions of TSS and downstream 2.5kb regions of TTS. Genes were categorized into two subgroups according to whether they harbor m^{6}A-marked upstream carRNAs (m^{6}A) or not (non-m^{6}A). For (A) and (B), $n = 2$ biological replicates. (**C**) Cell migration measured with wound healing assay of *METTL3* knockdown versus control HEC-1-A cells. Cells were treated with DMSO or HDAC inhibitor (HDACi), $n = 3$ biological replicates; error bars indicate mean ± S.E.M.

Additional Data Table S1.
Sequences of qPCR primers and gRNAs.

Additional Data Table S2.
Summary of sample information for high-through sequencing in this study.

References and Notes

1. D. Dominissini, S. Moshitch-Moshkovitz, S. Schwartz, M. Salmon-Divon, L. Ungar, S. Osenberg, K. Cesarkas, J. Jacob-Hirsch, N. Amariglio, M. Kupiec, R. Sorek, G. Rechavi, Topology of the human and mouse m^{6}A RNA methylomes revealed by m^{6}A-seq. *Nature* **485**, 201–206 (2012). doi:10.1038/nature11112 Medline

2. K. D. Meyer, Y. Saletore, P. Zumbo, O. Elemento, C. E. Mason, S. R. Jaffrey, Comprehensive analysis of mRNA methylation reveals enrichment in 3′ UTRs and near stop codons. *Cell* **149**, 1635–1646 (2012). doi:10.1016/j.cell.2012.05.003 Medline

3. M. Frye, B. T. Harada, M. Behm, C. He, RNA modifications modulate gene expression during development. *Science* **361**, 1346–1349 (2018). doi:10.1126/science.aau1646 Medline

4. I. A. Roundtree, M. E. Evans, T. Pan, C. He, Dynamic RNA modifications in gene expression regulation. *Cell* **169**, 1187–1200 (2017). doi:10.1016/j.cell.2017.05.045 Medline

5. G. Jia, Y. Fu, X. Zhao, Q. Dai, G. Zheng, Y. Yang, C. Yi, T. Lindahl, T. Pan, Y.-G. Yang, C. He, N^6-methyladenosine in nuclear RNA is a major substrate of the obesity-associated FTO. *Nat. Chem. Biol.* **7**, 885–887 (2011). doi:10.1038/nchembio.687 Medline

6. G. Zheng, J. A. Dahl, Y. Niu, P. Fedorcsak, C.-M. Huang, C. J. Li, C. B. Vågbø, Y. Shi, W.-L. Wang, S.-H. Song, Z. Lu, R. P. G. Bosmans, Q. Dai, Y.-J. Hao, X. Yang, W.-M. Zhao, W.-M. Tong, X.-J. Wang, F. Bogdan, K. Furu, Y. Fu, G. Jia, X. Zhao, J. Liu, H. E. Krokan, A. Klungland, Y.-G. Yang, C. He, ALKBH5 is a mammalian RNA demethylase that impacts RNA metabolism and mouse fertility. *Mol. Cell* **49**, 18–29 (2013). doi:10.1016/j.molcel.2012.10.015 Medline

7. X. Wang, Z. Lu, A. Gomez, G. C. Hon, Y. Yue, D. Han, Y. Fu, M. Parisien, Q. Dai, G. Jia, B. Ren, T. Pan, C. He, N^6-methyladenosine-dependent regulation of messenger RNA stability. *Nature* **505**, 117–120 (2014). doi:10.1038/nature12730 Medline

8. X. Wang, B. S. Zhao, I. A. Roundtree, Z. Lu, D. Han, H. Ma, X. Weng, K. Chen, H. Shi, C. He, N^6-methyladenosine modulates messenger RNA translation efficiency. *Cell* **161**, 1388–1399 (2015). doi:10.1016/j.cell.2015.05.014 Medline

9. W. Xiao, S. Adhikari, U. Dahal, Y.-S. Chen, Y.-J. Hao, B.-F. Sun, H.-Y. Sun, A. Li, X.-L. Ping, W.-Y. Lai, X. Wang, H.-L. Ma, C.-M. Huang, Y. Yang, N. Huang, G.-B. Jiang, H.-L. Wang, Q. Zhou, X.-J. Wang, Y.-L. Zhao, Y.-G. Yang, Nuclear m^{6}A reader YTHDC1 regulates mRNA splicing. *Mol. Cell* **61**, 507–519 (2016). doi:10.1016/j.molcel.2016.01.012 Medline

10. P. J. Batista, B. Molinie, J. Wang, K. Qu, J. Zhang, L. Li, D. M. Bouley, E. Lujan, B. Haddad, K. Daneshvar, A. C. Carter, R. A. Flynn, C. Zhou, K.-S. Lim, P. Dedon, M. Wernig, A. C. Mullen, Y. Xing, C. C. Giallourakis, H. Y. Chang, m^{6}A RNA modification controls cell fate transition in mammalian embryonic stem cells. *Cell Stem Cell* **15**, 707–719 (2014). doi:10.1016/j.stem.2014.09.019 Medline

11. S. Geula, S. Moshitch-Moshkovitz, D. Dominissini, A. A. F. Mansour, N. Kol, M. Salmon-Divon, V. Hershkovitz, E. Peer, N. Mor, Y. S. Manor, M. S. Ben-Haim, E. Eyal, S. Yunger, Y. Pinto, D. A. Jaitin, S. Viukov, Y. Rais, V. Krupalnik, E. Chomsky, M. Zerbib, I. Maza, Y. Rechavi, R. Massarwa, S. Hanna, I. Amit, E. Y. Levanon, N.

Amariglio, N. Stern-Ginossar, N. Novershtern, G. Rechavi, J. H. Hanna, m^{6}A mRNA methylation facilitates resolution of naïve pluripotency toward differentiation. *Science* **347**, 1002–1006 (2015). doi:10.1126/science.1261417 Medline

12. Y. Wang, Y. Li, J. I. Toth, M. D. Petroski, Z. Zhang, J. C. Zhao, *N*^{6}-methyladenosine modification destabilizes developmental regulators in embryonic stem cells. *Nat. Cell Biol.* **16**, 191–198 (2014). doi:10.1038/ncb2902 Medline

13. I. Ivanova, C. Much, M. Di Giacomo, C. Azzi, M. Morgan, P. N. Moreira, J. Monahan, C. Carrieri, A. J. Enright, D. O'Carroll, The RNA m^{6}A reader YTHDF2 is essential for the post-transcriptional regulation of the maternal transcriptome and oocyte competence. *Mol. Cell* **67**, 1059–1067.e4 (2017). doi:10.1016/j.molcel.2017.08.003 Medline

14. S. D. Kasowitz, J. Ma, S. J. Anderson, N. A. Leu, Y. Xu, B. D. Gregory, R. M. Schultz, P. J. Wang, Nuclear m^{6}A reader YTHDC1 regulates alternative polyadenylation and splicing during mouse oocyte development. *PLOS Genet.* **14**, e1007412 (2018). doi:10.1371/journal.pgen.1007412 Medline

15. Y. Wang, Y. Li, M. Yue, J. Wang, S. Kumar, R. J. Wechsler-Reya, Z. Zhang, Y. Ogawa, M. Kellis, G. Duester, J. C. Zhao, N^6-methyladenosine RNA modification regulates embryonic neural stem cell self-renewal through histone modifications. *Nat. Neurosci.* **21**, 195–206 (2018). doi:10.1038/s41593-017-0057-1 Medline

16. I. Barbieri, K. Tzelepis, L. Pandolfini, J. Shi, G. Millán-Zambrano, S. C. Robson, D. Aspris, V. Migliori, A. J. Bannister, N. Han, E. De Braekeleer, H. Ponstingl, A. Hendrick, C. R. Vakoc, G. S. Vassiliou, T. Kouzarides, Promoter-bound METTL3 maintains myeloid leukaemia by m^{6}A-dependent translation control. *Nature* **552**, 126–131 (2017). doi:10.1038/nature24678 Medline

17. B. Slobodin, R. Han, V. Calderone, J. A. F. O. Vrielink, F. Loayza-Puch, R. Elkon, R. Agami, Transcription impacts the efficiency of mRNA translation via co-transcriptional *N*^{6}-adenosine methylation. *Cell* **169**, 326–337.e12 (2017). doi:10.1016/j.cell.2017.03.031 Medline

18. M. Lubas, M. S. Christensen, M. S. Kristiansen, M. Domanski, L. G. Falkenby, S. Lykke-Andersen, J. S. Andersen, A. Dziembowski, T. H. Jensen, Interaction profiling identifies the human nuclear exosome targeting complex. *Mol. Cell* **43**, 624–637 (2011). doi:10.1016/j.molcel.2011.06.028 Medline

19. J. W. Jachowicz, X. Bing, J. Pontabry, A. Bošković, O. J. Rando, M.-E. Torres-Padilla, LINE-1 activation after fertilization regulates global chromatin accessibility in the early mouse embryo. *Nat. Genet.* **49**, 1502–1510 (2017). doi:10.1038/ng.3945 Medline

20. M. Percharde, C.-J. Lin, Y. Yin, J. Guan, G. A. Peixoto, A. Bulut-Karslioglu, S. Biechele, B. Huang, X. Shen, M. Ramalho-Santos, A LINE1-nucleolin partnership regulates early development and ESC identity. *Cell* **174**, 391–405.e19 (2018). doi:10.1016/j.cell.2018.05.043 Medline

21. A. Mayer, J. di Iulio, S. Maleri, U. Eser, J. Vierstra, A. Reynolds, R. Sandstrom, J. A. Stamatoyannopoulos, L. S. Churchman, Native elongating transcript sequencing reveals human transcriptional activity at nucleotide resolution. *Cell* **161**, 541–554 (2015). doi:10.1016/j.cell.2015.03.010 Medline

22. T. Nojima, T. Gomes, A. R. F. Grosso, H. Kimura, M. J. Dye, S. Dhir, M. Carmo-Fonseca, N. J. Proudfoot, Mammalian NET-Seq reveals genome-wide nascent transcription coupled to RNA processing. *Cell* **161**, 526–540 (2015). doi:10.1016/j.cell.2015.03.027 Medline

23. E. Pefanis, J. Wang, G. Rothschild, J. Lim, D. Kazadi, J. Sun, A. Federation, J. Chao, O. Elliott, Z.-P. Liu, A. N. Economides, J. E. Bradner, R. Rabadan, U. Basu, RNA exosome-regulated long non-coding RNA transcription controls super-enhancer activity. *Cell* **161**, 774–789 (2015). doi:10.1016/j.cell.2015.04.034 Medline

24. D. A. Bose, G. Donahue, D. Reinberg, R. Shiekhattar, R. Bonasio, S. L. Berger, RNA binding to CBP stimulates histone acetylation and transcription. *Cell* **168**, 135–149.e22 (2017). doi:10.1016/j.cell.2016.12.020 Medline

25. A. A. Sigova, B. J. Abraham, X. Ji, B. Molinie, N. M. Hannett, Y. E. Guo, M. Jangi, C. C. Giallourakis, P. A. Sharp, R. A. Young, Transcription factor trapping by RNA in gene regulatory elements. *Science* **350**, 978–981 (2015). doi:10.1126/science.aad3346 Medline

26. X. Wang, R. D. Paucek, A. R. Gooding, Z. Z. Brown, E. J. Ge, T. W. Muir, T. R. Cech, Molecular analysis of PRC2 recruitment to DNA in chromatin and its inhibition by RNA. *Nat. Struct. Mol. Biol.* **24**, 1028–1038 (2017). doi:10.1038/nsmb.3487 Medline

27. S. Rauch, C. He, B. C. Dickinson, Targeted m^6A reader proteins to study epitranscriptomic regulation of single RNAs. *J. Am. Chem. Soc.* **140**, 11974–11981 (2018). doi:10.1021/jacs.8b05012 Medline

28. J. Liu, M. A. Eckert, B. T. Harada, S.-M. Liu, Z. Lu, K. Yu, S. M. Tienda, A. Chryplewicz, A. C. Zhu, Y. Yang, J.-T. Huang, S.-M. Chen, Z.-G. Xu, X.-H. Leng, X.-C. Yu, J. Cao, Z. Zhang, J. Liu, E. Lengyel, C. He, m^6A mRNA methylation regulates AKT activity to promote the proliferation and tumorigenicity of endometrial cancer. *Nat. Cell Biol.* **20**, 1074–1083 (2018). doi:10.1038/s41556-018-0174-4 Medline

29. J. Wuarin, U. Schibler, Physical isolation of nascent RNA chains transcribed by RNA polymerase II: Evidence for cotranscriptional splicing. *Mol. Cell. Biol.* **14**, 7219–7225 (1994). doi:10.1128/MCB.14.11.7219 Medline

30. A. M. Bolger, M. Lohse, B. Usadel, Trimmomatic: A flexible trimmer for Illumina sequence data. *Bioinformatics* **30**, 2114–2120 (2014). doi:10.1093/bioinformatics/btu170 Medline

31. D. Kim, B. Langmead, S. L. Salzberg, HISAT: A fast spliced aligner with low memory requirements. *Nat. Methods* **12**, 357–360 (2015). doi:10.1038/nmeth.3317 Medline

32. H. Li, B. Handsaker, A. Wysoker, T. Fennell, J. Ruan, N. Homer, G. Marth, G. Abecasis, R. Durbin, 1000 Genome Project Data Processing Subgroup, The Sequence Alignment/Map format and SAMtools. *Bioinformatics* **25**, 2078–2079 (2009). doi:10.1093/bioinformatics/btp352 Medline

33. Y. Zhang, T. Liu, C. A. Meyer, J. Eeckhoute, D. S. Johnson, B. E. Bernstein, C. Nusbaum, R. M. Myers, M. Brown, W. Li, X. S. Liu, Model-based analysis of ChIP-Seq (MACS). *Genome Biol.* **9**, R137 (2008). doi:10.1186/gb-2008-9-9-r137 Medline

34. A. R. Quinlan, I. M. Hall, BEDTools: A flexible suite of utilities for comparing genomic features. *Bioinformatics* **26**, 841–842 (2010). doi:10.1093/bioinformatics/btq033 Medline

35. S. Anders, P. T. Pyl, W. Huber, HTSeq—A Python framework to work with high-throughput sequencing data. *Bioinformatics* **31**, 166–169 (2015). doi:10.1093/bioinformatics/btu638 Medline

36. M. D. Robinson, D. J. McCarthy, G. K. Smyth, edgeR: A Bioconductor package for differential expression analysis of digital gene expression data. *Bioinformatics* **26**, 139–140 (2010). doi:10.1093/bioinformatics/btp616 Medline

37. H. Huang, H. Weng, W. Sun, X. Qin, H. Shi, H. Wu, B. S. Zhao, A. Mesquita, C. Liu, C. L. Yuan, Y.-C. Hu, S. Hüttelmaier, J. R. Skibbe, R. Su, X. Deng, L. Dong, M. Sun, C. Li, S. Nachtergaele, Y. Wang, C. Hu, K. Ferchen, K. D. Greis, X. Jiang, M. Wei, L. Qu, J.-L. Guan, C. He, J. Yang, J. Chen, Recognition of RNA N^6-methyladenosine by IGF2BP proteins enhances mRNA stability and translation. *Nat. Cell Biol.* **20**, 285–295 (2018). doi:10.1038/s41556-018-0045-z Medline

38. B. Langmead, C. Trapnell, M. Pop, S. L. Salzberg, Ultrafast and memory-efficient alignment of short DNA sequences to the human genome. *Genome Biol.* **10**, R25 (2009). doi:10.1186/gb-2009-10-3-r25 Medline

39. S. Heinz, C. Benner, N. Spann, E. Bertolino, Y. C. Lin, P. Laslo, J. X. Cheng, C. Murre, H. Singh, C. K. Glass, Simple combinations of lineage-determining transcription factors prime cis-regulatory elements required for macrophage and B cell identities. *Mol. Cell* **38**, 576–589 (2010). doi:10.1016/j.molcel.2010.05.004 Medline

40. W. A. Whyte, D. A. Orlando, D. Hnisz, B. J. Abraham, C. Y. Lin, M. H. Kagey, P. B. Rahl, T. I. Lee, R. A. Young, Master transcription factors and mediator establish super-enhancers at key cell identity genes. *Cell* **153**, 307–319 (2013). doi:10.1016/j.cell.2013.03.035 Medline

41. Y. Liao, G. K. Smyth, W. Shi, featureCounts: An efficient general purpose program for assigning sequence reads to genomic features. *Bioinformatics* **30**, 923–930 (2014). doi:10.1093/bioinformatics/btt656 Medline

42. R. Hubley, R. D. Finn, J. Clements, S. R. Eddy, T. A. Jones, W. Bao, A. F. A. Smit, T. J. Wheeler, The Dfam database of repetitive DNA families. *Nucleic Acids Res.* **44**, D81–D89 (2016). doi:10.1093/nar/gkv1272 Medline

43. D. W. Huang, B. T. Sherman, R. A. Lempicki, Systematic and integrative analysis of large gene lists using DAVID bioinformatics resources. *Nat. Protoc.* **4**, 44–57 (2009). doi:10.1038/nprot.2008.211 Medline

44. D. W. Huang, B. T. Sherman, R. A. Lempicki, Bioinformatics enrichment tools: Paths toward the comprehensive functional analysis of large gene lists. *Nucleic Acids Res.* **37**, 1–13 (2009). doi:10.1093/nar/gkn923 Medline